

---

## Simulating sediment supply from the Congo watershed over the last 155 ka

Molliex Stéphane <sup>1,\*</sup>, Kettner Albert J. <sup>2</sup>, Laurent Dimitri <sup>3</sup>, Droz Laurence <sup>6</sup>, Marsset Tania <sup>3</sup>, Laraque Alain <sup>4</sup>, Rabineau Marina <sup>6</sup>, N'Kaya Guy D. Moukandi <sup>5</sup>

<sup>1</sup> Univ Bretagne Occidentale, CNRS, IUEM, Lab Geosci Ocean, Labex Mer, UMR 6538, F-29280 Plouzane, France.

<sup>2</sup> Univ Colorado, Inst Arctic & Alpine Res, CSDMS, Dartmouth Flood Observ, Boulder, CO 80309 USA.

<sup>3</sup> IFREMER, UR Geosci Marines, BP 70, F-29280 Plouzane, France.

<sup>4</sup> OMP, F-31400 Toulouse, France.

<sup>5</sup> Univ Marien Ngouabi, LMEI CUSI ENSP, BP 69, Brazzaville, Rep Congo.

\* Corresponding author : Stéphane Molliex, email address : [smolliex@gmail.com](mailto:smolliex@gmail.com)

---

### Abstract :

The Congo River is the world's second largest river in terms of drainage area and water discharge. Monitored for decades, a large dataset is available, onshore for both the hydrology and sediment load, and offshore by many paleo-environmental proxies compiled at the Late-Quaternary time-scale. These numerous data allow for accurate calibration of numerical modeling. In this study, we aim to numerically quantify the evolution of sediment supply leaving the tropical Congo watershed during the last 155 ka and to decipher the forcing parameters that control this sediment supply over glacial/interglacial stages. For this, a modified version of the model HydroTrend, that besides morphologic, climatic, hydrologic, lithologic, land cover and anthropogenic factors now also considers sediment deposition on the floodplain, is used. In addition, a method to quantify the impact of natural vegetation changes is developed.

Simulations match well the present-day observed data. They indicate that a significant portion of suspended sediments is trapped on the floodplain. Long-term simulations indicate that environmental changes between glacial and interglacial stages account for a 30% maximum variation of sediment supply. Climatic changes - precipitation and temperature, account for a maximum decrease in sediment supply of 20% during cold periods while conversely, induced land cover changes (loss of forest during colder and dryer stages) lead to enhanced sediment supply up to 30%. Over a longer period, the average sediment supply remained almost constant during glacial and interglacial periods, while peaks may have occurred during a warming period, just before forests had time to recover the catchment, i.e. during post-glacial periods. These moderate changes in sediment export, despite major changes in climate and vegetation cover, can be explained by the efficiency of sediment trapping of large tropical catchments that buffer fluvial fluxes towards the ocean.

**Keywords :** Glacial/interglacial, Sediment supply modeling, HydroTrend, Vegetation dynamics, Equatorial Africa, Congo watershed, Weathering, Hydrology

42 Understanding factors and processes controlling sediment yield is crucial for a comprehensive baseline  
43 in global denudation rates, fluvial sedimentary archives, biochemical cycles and human impact on  
44 sediment fluxes (e.g. Meybeck, 2003; Walling, 2006; Syvitski and Milliman, 2007). Sediment yield  
45 can be expressed as a function of various factors including catchment morphology (area, relief, slope),  
46 lithology, climatic conditions, tectonics, vegetation, land use, impact of reservoirs (e.g. de Vente and  
47 Poesen, 2005; Syvitski and Milliman, 2007; Pelletier, 2012; Vanmaercke et al., 2014). However, the  
48 quantification of evolution of sediment yields over time remains a challenge because of the number of  
49 processes, the complexity, and the feedbacks of processes involved both on soil denudation and fluvial  
50 sediment transport (Picouet et al., 2001). In addition, the relative importance of forcing parameters  
51 depends on the size of the catchment and the climatic and tectonic context of its setting and is often  
52 poorly understood.

53 Large tropical catchments contain some of the richest ecosystems on Earth and provide a large part of  
54 nutrients to the oceans. Tropical zones have the largest land mass on Earth, a high transport capacity,  
55 high erosion rates due to biogeochemical weathering, and thus sediment loads are enhanced by the  
56 humid and warm climate (e.g. Xu, 2003; Zhu et al., 2007; Syvitski et al., 2017). Therefore large  
57 tropical catchments are playing an essential role in both terrestrial and marine ecosystems.  
58 Nevertheless, processes controlling sediment fluxes to the ocean are poorly understood and because of  
59 basin size, accurate quantification of these processes over time is often challenging to perform.

60 The Congo River is the world's second largest river in terms of both drainage area ( $3.7 \cdot 10^6 \text{ km}^2$ ) and  
61 water discharge ( $41,000 \text{ m}^3 \text{ s}^{-1}$ ) (Laraque et al., 2013). Its catchment can be considered as the most  
62 pristine major tropical watershed because it has for example far fewer dams in comparison with other  
63 large tropical watersheds such as the Amazon (Latrubesse et al., 2017) or Mekong Rivers (Ellis et al.,  
64 2012; Winemiller et al., 2016). However, because it is challenging to acquire *in-situ* data, the Congo  
65 basin has experienced much less scientific attention in basin hydrology and sediment supply than other  
66 large tropical catchments (Alsdorf et al., 2016). Unlike other major rivers, the contemporary Congo  
67 River has always maintained a connection with its deep-sea canyon, allowing for efficient transfer of

68 Total Suspended Sediment (TSS) directly to the abyssal plain (Rabouille et al., 2009; Vangriesheim et  
69 al., 2009). Moreover, Gingele et al. (1998) showed by studying smectite cristallinity that at least 95%  
70 of sediment deposited in the deep-sea fan is directly provided by the Congo River, with aeolian  
71 contribution being limited. These characteristics make a direct comparison between sediment supply  
72 exported from the catchment and the sediment volume deposited in the deep-sea fan possible.

73 Better understanding of the main controlling factors of sediment yields in Africa is also of interest  
74 from a societal perspective. Recent population growth and climatic changes in Africa have important  
75 impacts on land cover changes and water resources (e.g. Barnes, 1990; Bruijnzeel, 2004; Zhang et al.,  
76 2006; Reichenstein et al., 2013). Reliable information on the variability over time in sediment yield  
77 and its sensitivity to land cover or climate changes is therefore crucial for sustainable catchment  
78 management (Vanmaercke et al., 2014).

79 Recently, development of remote sensing tools have allowed for better understanding of the Congo's  
80 terrestrial water dynamics (Jung et al., 2010; Beighley et al., 2011; O'Loughlin et al., 2013; Lee et al.,  
81 2011; 2014; 2015). Moreover, numerical models such as HydroTrend, based on empirical equations  
82 can simulate water and sediment discharge of watersheds and have proven to be able to successfully  
83 reproduce basin hydrology over geological times with high accuracy (e.g. Syvitski and Miliman,  
84 2007). These are thus reliable tools for quantifying the role of environmental forcing on fluvial  
85 processes, in particular since only 10 % of rivers have observational time series of sediment delivery  
86 to the ocean (Syvitski et al., 2005). Of those, few records reach more than a century, which is too short  
87 to fully comprehend and unravel processes influencing the fluvial sediment fluxes (Wilby et al., 1997).

88 However, modeling the Congo's catchment sediment supply towards the ocean is challenging because  
89 (i) the size of the catchment, which includes several climatic zones; (ii) the strong variability of land  
90 cover over time due to its sensitivity to climate changes, and (iii) of net depositional areas in the  
91 catchment that are not always clearly identifiable.

92 In this study, we simulate the water and suspended sediment discharge exported from the Congo's  
93 River basin over the last 155 ka by applying the hydrological transport model HydroTrend, of which  
94 the sediment module encompasses the empirical BQART function (Syvitski et al., 1998; Kettner and  
95 Syvitski, 2008). This quantification is based on a calibration by *in-situ* present-day data. The  
96 variability of water and sediment discharge over the last 155 ka is then modeled from this calibration  
97 by using available environmental proxies. These simulations aim to improve our understanding of the  
98 factors controlling sediment yield of the Congo catchment and help address societal challenges. In  
99 detail, we aim to better understand how the suspended sediment supply varies over one full climatic  
100 glacial/interglacial cycle with a focus on transitions. Which are the parameters controlling these  
101 variations and how do they control suspended sediment fluxes? We also validate our long-term

102 sediment flux simulations with published denudation and weathering rates, volumes of sediment  
103 deposited offshore and basic weathering proxies determined from marine cores.

## 104 **2- Environmental setting**

105 The 4,700 km long Congo River drains 3.7 millions of km<sup>2</sup> of the center of equatorial Africa (Fig. 1),  
106 and lies on both sides of the equator. Its heart is constituted by a vast (about 50% of the total drainage  
107 area), low gradient (at some locations the slope is less than a few centimeter per kilometer) and  
108 shallow perched basin (with altitudes ranging from 300 to 500 m) called “Cuvette Centrale” (Fig. 1A,  
109 1B and 1C). This depression, is the surface expression of a Cenozoic basin, and is surrounded by  
110 moderately elevated hills (1000 to 1500 m of elevation) to the North and South, and by a mountain  
111 range to the East (the western shoulder of the East African Rift), where elevations reach up to 4100 m  
112 (Fig. 1B). These reliefs mainly consist of crystalline basement (e.g. Lee et al., 2015). Terrains with  
113 elevations higher than 2000 m only represent 0.4% of the drainage area. Drainage area located in the  
114 southern hemisphere represents about 60% of the total drainage area, with a mean elevation of about  
115 200 m higher than the elevation of the drainage area located in the northern hemisphere (Fig. 1A and  
116 1B). The main tributaries of the Congo River are the Oubangui, the Sangha, the group of Batékés  
117 Rivers on its right bank, and the Kasai River on its left bank (Fig. 1). The headwaters of the Congo  
118 catchment contain the world’s second largest lake by volume and depth (Lake Tanganyika), which  
119 holds approximately 17% of the world’s fresh water volume (Coulter, 1991) and traps the majority of  
120 sediments provided by the upstream part of the catchment (Sichingabula, 1999). In the Cuvette  
121 Centrale, two very shallow (3 to 8 m deep) lakes (Tumba and Mai Ndombé) extend for more than  
122 3000 km<sup>2</sup> and are situated on the left bank of the Congo River (Laraque et al., 1998). These lakes, as  
123 well as the “Cuvette Centrale”, which is almost permanently flooded, trap a large part of the  
124 suspended sediment load. The Congo River delivers water and sediment to the Atlantic Ocean and is  
125 directly and permanently connected to an active deep-sea fan through the 1,135 km-long deeply  
126 incised submarine Congo Canyon and channels (Babonneau et al., 2002). This hydrographic network  
127 remained relatively stable throughout the Quaternary despite sea-level and climatic changes  
128 (Guillocheau et al., 2015; Flügel et al., 2015).

129 Currently, the Congo Basin experiences a humid tropical climate with three main climatic zones: a)  
130 equatorial humid in the center of the basin on both sides of the Equator, b) tropical humid with a  
131 monsoon season at higher latitudes, and c) tropical semi-arid with a dry season on the northern and  
132 southern catchment boundaries (Kottek et al., 2006). The mean annual precipitation is 1,630 mm with  
133 a mean temperature of about 24°C at Brazzaville (Bultot, 1972; Alsdorf et al., 2016) (Fig. 2A; Fig.  
134 2B). Vast areas of the central Congo Basin do not experience a dry season, whereas the highlands  
135 experience two wet and dry seasons (Boyer et al., 2006). The Congo River crosses the Equator twice  
136 and, as a result, experiences always a rainy season somewhere in its basin during the year (Fig. 2A and

137 2D). The wet season for the southerly flowing tributaries is from April to September (e.g. the  
138 Oubangui River) and for the northerly flowing tributaries from October to May (e.g. the Kasai River).  
139 This results in a typically equatorial hydrological regime (Rodier, 1964; Martins and Probst, 1991)  
140 with limited monthly discharge fluctuations (Fig. 2E; 3A). As an example, for the Congo only two  
141 minor peak events in December and May and two minor low flow events in August and March occur  
142 (Coynel et al., 2005; Laraque et al., 2009; 2013a) (Fig. 3A). Intrinsically, the Congo River experiences  
143 probably the most regular and uniform hydrologic regime on Earth since its mean monthly discharge  
144 ratio (maxQ/minQ) is close to 2 and the extreme monthly discharges, recorded from 1902 onwards,  
145 range only from 23,000 to 75,500 m<sup>3</sup> s<sup>-1</sup> (Alsdorf et al., 2016). The inter-annual ratio is only 1.65 with  
146 annual discharges ranging from 33,300 to 55,200 m<sup>3</sup> s<sup>-1</sup> (Alsdorf et al., 2016). The height of the water  
147 table, inferred from lake levels (Crétau et al., 2011; Becker et al., 2014) varies by 80 mm during the  
148 year and follows the same trend as the water balance (Precipitation minus Evapotranspiration) (Fig.  
149 2E). Water specific discharge (runoff) stays however almost constant (35 ± 5 mm), highlighting a  
150 good relationship between surface and underground water that allows for buffering the monthly river  
151 discharge and explains part of the low variability of the hydrologic system.

152 The “Cuvette Centrale” is mainly covered by evergreen and swamp forest and surrounded by savannah  
153 vegetation (De Namur, 1990) (Fig. 2C and Fig. 2F). During the wet season, most of these forests are  
154 flooded, while during the dry season, they partially or completely dry (Laraque et al., 1998; Coynel et  
155 al., 2005). Anthropogenic disturbances such as sewage inputs, intensive agriculture, deforestation, and  
156 dams have not yet had a significant impact on the Congo River, which has therefore not developed any  
157 of the global change syndromes observed for most of the world’s largest basins (Meybeck, 2003;  
158 Coynel et al., 2005). And therefore, the sediment dynamics are still mostly in a natural state.

159 The Congo River currently transports a total of 87 Mt yr<sup>-1</sup> of matter to the ocean (Laraque et al. 2009,  
160 2013b). Only one third is constituted by suspended sediment load (SSL) while the main part of matter  
161 exported is dissolved (Laraque et al. 2009, 2013b) (Fig. 3B). No accurate data is available for bed  
162 load. As for the water discharge, the mean monthly suspended sediment load is also uniform. The total  
163 dissolved matter is well correlated to the water discharge, conversely to the SSL (Fig. 3C; 3D).  
164 Because of the scarcity of high slope areas in the catchment (less than 0.0005 % of the drainage area  
165 has slopes higher than 45°), potential landslides triggered by earthquakes in upstream Congo are  
166 unlikely to significantly impact the total suspended sediment load of the catchment.

### 167 ***3- Data and Method***

168 Our simulations were performed by removing part of the Congo Basin located upstream of Lake  
169 Tanganyika. The area upstream of Lake Tanganyika, that mainly drains the East-African Rift System,  
170 does not significantly contribute to the sediment flux towards the ocean as this lake traps large

171 portions of the upstream sediment supply (Sichingabula, 1999). For this study, the Congo River outlet  
 172 was considered at Brazzaville, about 480 km upstream the Congo's actual river mouth (Fig. 1A, 1C).  
 173 This in order to (i) calibrate our simulations with *in-situ* data available at the Brazzaville's gauging  
 174 station; and (ii) avoid the potential effect of sea-level fluctuations over glacial-interglacial stages to the  
 175 catchment, since the erosive regression of the Congo channel due to sea-level regressions does not  
 176 affect the catchment upstream Brazzaville, as shown by the location of the major knickpoint in the  
 177 longitudinal profile of the river just downstream Brazzaville (Fig. 1C). Our strategy was to calibrate  
 178 our simulations using present-day data, before simulating over two different timescales, the last 23 ka  
 179 and the last 155 ka, by integrating environmental changes, inferred from both marine and continental  
 180 proxies available for the study area. Simulations over these two different timescales aimed to test the  
 181 sensibility of the model resolution and also to study the the impact of different controlling factors  
 182 during climate transitions periods. Furthermore, we included to the classic HydroTrend model the  
 183 possibility to consider trapping in the alluvial plain, when the discharge exceeds bankfull. We also  
 184 developed a new methodology to consider vegetation cover variations that can occur between glacial  
 185 and interglacial periods.

### 186 3.1 General principles of HydroTrend

187 The HydroTrend model allows for daily simulation of discharge and sediment load leaving a river  
 188 system with high accuracy over long periods of time (Syvitski et al., 1998). The model incorporates  
 189 basin properties and biophysical processes to compute the hydrological balance (Kettner and Syvitski,  
 190 2008). For long-term simulations, HydroTrend has proven to be able to reproduce reliable fluvial  
 191 sediment yield if appropriate assumptions about past climate and land use are made (Syvitski and  
 192 Morehead, 1999; Kettner and Syvitsky, 2009). The structure and modules of HydroTrend have been  
 193 described in detail by Syvitski et al. (1998) and Kettner and Syvitski (2008), and will not be iterated  
 194 here. However, key equations to compute water discharge, sediment load, and trapping efficiency will  
 195 be described below.

196 Based on the classic water balance equation, fluvial water discharge ( $Q$ ) is determined by basin area  $A$   
 197 ( $\text{km}^2$ ), precipitation  $P$  ( $\text{m yr}^{-1}$ ), evapotranspiration  $Ev$  ( $\text{m}^3 \text{s}^{-1}$ ) and water storage as groundwater and  
 198 its release  $Sr$  ( $\text{m}^3 \text{s}^{-1}$ ) (Eq. 1).

$$199 \quad Q = A \sum_{i=1}^{ne} (P_i - Ev_i \pm Sr_i) \quad (\text{Eq. 1})$$

200 Here  $ne$  is the number of simulated epochs (time periods with more or less similar or linear changing  
 201 environmental conditions), each including multiple years, and  $i$  is the daily time step. Following Eq.  
 202 (1), five hydrological processes are taken into consideration: rain ( $Q_r$ ), snowmelt ( $Q_n$ ), glacial melt  
 203 ( $Q_{ice}$ ), evaporation ( $Q_{Ev}$ ) and groundwater discharge ( $Q_g$ ) (all in  $\text{m}^3 \text{s}^{-1}$ ) (Eq. 2):

$$204 \quad Q = Q_r + Q_n + Q_{ice} - Q_{Ev} \pm Q_g \quad (\text{Eq. 2})$$

205 The long-term suspended sediment load  $\bar{Q}_s$  ( $\text{kg s}^{-1}$ ) is computed by applying the semi-empirical  
 206 BQART equation described by Syvitski and Milliman (2007) (Eq. 3):

$$207 \quad \bar{Q}_s = \omega B \bar{Q}^{0.31} A^{0.5} \bar{R} T \quad (\text{Eq. 3})$$

208 The B term (non-dimensional) being estimated as:

$$209 \quad B = IL(1 - T_e)E_h \quad (\text{Eq. 4})$$

210 where  $\omega$  is the proportionality coefficient defined to be  $0.02 \text{ kg s}^{-1} \text{ km}^{-2} \text{ }^\circ\text{C}^{-1}$  (Syvitski and Milliman,  
 211 2007),  $\bar{Q}$  and  $\bar{R}$  are respectively non-dimensional water discharge at the river mouth and maximum  
 212 basin relief, following the procedure as  $\bar{Q} = \left(\frac{Q}{Q_0}\right)$  and  $\bar{R} = \left(\frac{R}{R_0}\right)$ , where  $Q_0$  is equal to  $1 \text{ m}^3 \text{ s}^{-1}$ , and  $R_0$   
 213 equals 1 m.  $T$  is the temperature at the basin outlet ( $^\circ\text{C}$ ).  $I$ ,  $L$ ,  $T_e$ , and  $E_h$  are non-dimensional  
 214 parameters, where  $I$  is a glacial erosion factor to represent the impact of glacial erosion processes,  $L$  is  
 215 the basin-averaged lithology factor to express the hardness of rock, and  $T_e$  is the trapping efficiency by  
 216 natural and/or human reservoirs.  $E_h$  is the soil erosion factor related to human activities (Syvitski and  
 217 Milliman, 2007; Kettner and Syvitski, 2008) which is adapted for our case to consider vegetation  
 218 changes (see section 3.3.2 for more details).

219 To generate daily SSL fluxes, a stochastic model (Psi) is applied (Eq. 5; Morehead et al., 2003).

$$220 \quad \left(\frac{Q_{s_i}}{\bar{Q}_s}\right) = \psi_i \left(\frac{Q_i}{\bar{Q}}\right)^C \quad i = 1 : m \quad (\text{Eq. 5})$$

221 where  $m$  is the total number of days ( $i$ ) being modeled per epoch. The Psi model captures the inter-  
 222 and intra-annual variability of SSL leaving the river mouth following Eqs. (6) to (9) (Morehead et al.,  
 223 2003; Syvitski et al., 2005):

$$224 \quad E(\psi) = 1 \quad (\text{Eq. 6})$$

$$225 \quad \sigma(\psi) = 0.763(0.99995)^{\bar{Q}} \quad (\text{Eq. 7})$$

$$226 \quad E(C) = 1.4 - 0.025T + 0.00013R + 0.145 \ln(\bar{Q}_s) \quad (\text{Eq. 8})$$

$$227 \quad \sigma(C) = 0.17 + 0.00000183\bar{Q} \quad (\text{Eq. 9})$$

228  $E$  and  $\sigma$  denote respectively the mean and standard deviation of a random variable  $\Psi$ . The random  
 229 variable changes on a daily time step and has a log-normal distribution.  $C$  is a normal distributed  
 230 rating coefficient that varies over a time step of one year (Syvitsky et al., 2000). For these two  
 231 variables, the standard deviation depends on the mean discharge, with a power relation for  $\psi$ . These  
 232 equations imply that small rivers have a larger variance in  $C$ , while larger rivers have a smaller  
 233 variance. Notice that for short-term simulations (years to decades), because of the nature of  
 234 incorporated variability (Eq. 5 to 9), the daily mean suspended sediment load  $Q_{s_i}$  might not exactly  
 235 match the long-term mean suspended sediment load  $\bar{Q}_s$  as computed by BQART (Eq. 3). However,  
 236 these two parameters converge in long-term simulations (hundreds to thousands of years).

237 Because of the basin size and insignificant annual variability in discharge and sediment load of the  
 238 Congo watershed,  $\sigma(C)$  (Eq. 9), using Morehead et al. (2003) provided a significant higher annual  
 239 variability compared to field observations. We recalculate the  $E(C)$  parameter specifically for the

240 Congo based on 16 years of regularly monitoring of annual sediment load data (PEGI program,  
 241 Laraque et Orange, 1996; HYBAM, 2016). The observed annual standard deviation is 12 % while Eq.  
 242 9 predicts about 40 %. We thus recalibrated Eq. 9 to better reflect variations in sediment for the Congo  
 243 River (Eq. 10):

$$244 \sigma(C) = 0.17 + 0.00000056\bar{Q} \quad (\text{Eq. 10})$$

245 The trapping efficiency  $T_e$  by natural reservoirs larger than  $0.5 \text{ km}^3$ , such as lakes, is calculated by  
 246 HydroTrend using the equation of Brune (1953) following Vörösmarty et al. (1997) when multiple  
 247 reservoirs are represented in a catchment:

$$248 T_e = \sum_{j=1}^m \left( 1 - \frac{0.05}{\sqrt{\Delta\tau_j}} \right) \quad (\text{Eq. 11})$$

249 Here  $\Delta\tau_j$  is the approximated residence time per sub-basin  $j$  and is estimated by

$$250 \Delta\tau_j = \frac{\sum_i^{n_i} V_i}{Q_j} \quad (\text{Eq. 12})$$

251 where  $V_i$  is the operational volume of the reservoir  $i$ , and  $Q_j$  is the discharge at the mouth of each sub-  
 252 basin  $j$ . Specifically to this study, we included in the model the possibility of additional trapping by  
 253 floodplains and wetlands. Many large catchments contain alluvial plains. When bankfull discharges  
 254 are exceed, sediment can be trapped within an alluvial plain. For the model, we considered that as the  
 255 discharge exceeds the bankfull threshold at a certain location (based on upstream area or certain  
 256 elevation in the drainage basin), sediment load is trapped on the floodplain ( $Q_{sibk}$ ) which is estimated  
 257 as:

$$258 Q_{sibk} = (Q_i - Q_{bk}) \times C_{si} \quad (\text{Eq. 13})$$

259 where the accessible water is daily calculated as total discharge ( $Q_i$ ) minus the bankfull threshold  
 260 ( $Q_{bk}$ ), and  $C_{si}$  is the daily sediment concentration. When the bankfull threshold is reached, we assume  
 261 that 100% of suspended sediments is deposited in the floodplain.

### 262 *3.2 Input parameters for short-term calibration.*

263 The morphological characteristics of the catchment, including river length, drainage area, the delta  
 264 slope, hypsometry, latitude, location of reservoirs, are extracted from the Shuttle Radar Topography  
 265 Mission Digital Elevation Model (SRTM DEM) with a spatial resolution of 30 arc-sec (Farr et al.,  
 266 2007). For hydrological properties, the average velocity of the Congo River at its main Maluku  
 267 Trechot gauging station (30 km upstream Brazzaville, Fig. 1) is  $1.23 \text{ m s}^{-1}$  (Laraque et al., 1995).  
 268 Groundwater storage ( $350 \pm 250 \text{ km}^3$ ), groundwater coefficient ( $15,000 \text{ m}^3 \text{ s}^{-1}$ ) and groundwater  
 269 exponent (1.4) are deduced from satellite-inferred lakes level fluctuations (HydroWeb database:  
 270 <http://www.legos.obs-mip.fr/en/soa/hydrologie/hydroweb/>; Crétaux et al., 2011; Becker et al., 2014).  
 271 The mean saturated hydraulic conductivity, related to soil texture is chosen to be  $315 \text{ mm/day}$ ,  
 272 corresponding to a moderate coarse sandy loam (Bear, 1972). A lithology factor of 0.5 ( $L$ ) is assigned



273 using the classification scheme of Syvitski and Milliman (2007). All input parameters used are  
274 summarized in Table 1.

275 Mean monthly temperatures at Brazzaville are compiled from the Worldclim database (Hijmans et al.,  
276 2005). Mean monthly precipitations are compiled both from the Tropical Rainfall Monitoring Mission  
277 (TRMM) (Wang et al., 2014) and from 277 *in-situ* climate stations compiled in the SIEREM database  
278 (Boyer et al., 2006) (locations are provided in Fig. 2A). This compilation highlights a good correlation  
279 between monthly precipitation and their standard deviation at the basin scale ( $R^2 = 0.9$ ), which  
280 suggests a low inter-annual variability and allows for the determination of the temporal standard  
281 deviation of precipitation applied to TRMM data. For the Congo basin, present-day Equilibrium-Line  
282 Altitude (ELA) of glaciers is about 4500 m (Osmaston and Harrison, 2005). Glacial erosion is thus  
283 currently negligible since only an insignificant part of the Congo catchment lies above this elevation.

### 284 *3.3 Input parameter for long-term simulations*

285 Since the hydrographic network remained almost unchanged (Flügel et al., 2015) and tectonics are  
286 stable throughout the Quaternary (Guillocheau et al., 2015), we can assume that only climate and land  
287 cover significantly influence water and sediment discharge during the last 155 ka. Given the high  
288 temporal resolution of the input data, the resolution of our simulations can be constrained to 200 years  
289 for the 0-23 ka period and 1,000 years for the 0-155 ka simulation.

#### 290 *3-3-1- Climate changes*

291 Past precipitation and temperature can be reconstructed using proxies from local marine cores and  
292 global climatic models (Fig. 4). For precipitation, we use the  $\delta^{18}\text{O}$  curve compiled from core MD03-  
293 2707 (Weldeab et al., 2007) located in the Gulf of Guinea about 1000 km NW of the Congo's outlet.  
294 This proxy is representative of the intensity of the West African Monsoon (Weldeab et al., 2007,  
295 Caley et al., 2011). For temperature, we use interpolations of Weijers et al. (2007), who directly  
296 interpolated the mean atmospheric temperature (MAT) from the Methylation index of Branched  
297 Tetraethers (MBT) and the Cyclisation ratio of Branched Tetraethers (CBT) in core GeoB6518-1 for  
298 the last 25 ka, located close to the Congo River outlet (Fig. 1). In addition to these data, for ages older  
299 than 25 ka, we used the Sea Surface Temperature curve (SST) provided by Weldeab et al. (2007) from  
300 core MD03-2707, since a correlation can be made at these latitudes between sub-surface marine and  
301 aerial temperatures (Weaver et al., 2001). These data were then calibrated in terms of annual rainfall  
302 and temperature by using present-day and Last Glacial Maximum (LGM) global climatic models  
303 (CCSM4; Gent et al., 2011) (Fig. 4). Monthly variations are calibrated with simulations of Kutzbach et  
304 al., (1998) and Jolly et al., (1998). A first order variation of ELA is interpolated from local estimations  
305 at LGM of Osmaston and Harrison (2005), following the intensity of Marine Isotopic Stages (Lisiecki  
306 and Raymo, 2005). Note that less than 1 % of the catchment is concerned by glacial erosion during the

307 coldest phases (Osmaston and Harrison, 2005). Therefore, glacial erosion has only a limited impact  
308 during the cold stages on the fluvial sediment flux.

### 309 3-3-2- Land cover changes

310 Long-term land cover changes are constrained using recent data as well as a detailed pollen study of  
311 core KZaï-02 (Dalibard et al., 2014), collected in 1998 on the Congo deep-sea fan, 248 km off the  
312 Congo River mouth, during the ZaiAngo1 cruise (Savoie et al., 1998) (Fig. 1) to identify historical  
313 land cover changes. In order to quantify the impact of these changes in our simulations, we used an  
314 approach based both on a satellite derived land cover map (GLC-SHARE; Latham et al., 2014) and on  
315 monthly NDVI maps MOD13A3 provided by NASA  
316 ([https://lpdaac.usgs.gov/dataset\\_discovery/modis/modis\\_products\\_table/mod13a3](https://lpdaac.usgs.gov/dataset_discovery/modis/modis_products_table/mod13a3); Huete et al., 2002)  
317 (Fig. 5). NDVI (Normalized Difference Vegetation Index) (Tucker, 1979) is a widely used index in  
318 remote sensing studies (e.g. Xie et al., 2008). It is based on green vegetation and varies between 0 for  
319 bare soil to 1 if the soil is entirely covered, so protected by vegetation (e.g. Crippen, 1990). We  
320 compiled a mean annual NDVI map for the Congo catchment by averaging 12 contiguous monthly  
321 NDVI maps MOD13A3 (period 2000-2001). Annual NDVI ranges from 0.35 for the sparsest  
322 grasslands and crops to 0.85 for the densest rainforests (Fig. 5C). We then computed the relationship  
323 between mean annual value of NDVI ( $NDVI_y$ ) and the proportion of forested areas for 100 x 100 km  
324 tiles in the catchment  $F_s$  (Fig. 5D). A correlation of  $R^2 = 0.52$  was found between forests and the  
325  $NDVI_y$ . This relationship is stronger if only forests located below 900 m of elevation are involved ( $R^2$   
326 = 0.68) (Fig. 5D), the correlation equation being:

$$327 \quad NDVI_y = 0.00187 \times F_s + 0.574 \quad (\text{Eq. 14})$$

328 Within the catchment, the elevation of 900 m corresponds to the lowest limit of mountainous type  
329 forests. We also compiled an evolution curve of the percentage of non-mountainous forests in the  
330 catchment using pollen data (Dalibard et al., 2014) and determined equivalent paleo-NDVI values  
331 from each epoch (age step) by using the correlation equation (Eq. 14) (Fig. 4E; 4F).

332 We can then determine a soil cover factor  $C_f$  from these paleo-NDVI values.  $C_f = 0$  if vegetation cover  
333 is negligible (i.e. bare soil), and  $C_f = 1$  if the vegetation entirely covers the soil. A maximum soil cover  
334 factor  $C_f$  can be determined by using the maximum amplitude of present-day  $NDVI_y$  values (i.e. 0.85  
335 for densest rainforest and 0.35 for sparsest grasslands and crops) and assuming that  $C_{f_{max}} = 1$  for the  
336 highest NDVI value (0.85; 100 % of forests) and  $C_{f_{max}} = 0$  for the lowest NDVI value (0.35; 0% of  
337 forests) (Fig. 4F). The minimum soil cover factor can be calculated from the amplitude of NDVI  
338 determined from the correlation between present-day NDVI and proportion of forest (eq. 14),  
339 assuming that  $C_{f_{min}} = 1$  for 100 % of forests (NDVI = 0.76) and  $C_{f_{min}} = 0$  for 0 % of forest (NDVI =  
340 0.57). These values can be assumed as minimum because where there is no forest nowadays,

341 vegetation is mainly constituted by savannah. But during colder periods, such as during the LGM,  
342 non-forested vegetation was probably much sparser, with a lower NDVI value.

343 In that case,  $C_{max}$  and  $C_{min}$  are thus calculated as following:

$$344 \quad C_{f_{max}} = (0.85 - 0.35)F + 0.35 \quad (\text{Eq. 15a})$$

$$345 \quad C_{f_{min}} = (0.76 - 0.57)F + 0.57 \quad (\text{Eq. 15b})$$

346 This parameter is integrated in the BQART equation by using the erosion factor parameter  $Eh$  (Eq. 4),  
347 such that:

$$348 \quad E_h = (1 - Cf) \times 2 \quad (\text{Eq. 16})$$

349 We add a factor of 2 to ensure that a normal erosion factor ( $Eh = 1$ ) corresponds to a moderate  
350 vegetation cover, which has a  $NDVI_y$  of 0.5.

351 Ratios of erosion factors between grassland, savannah and non-mountainous forests are consistent  
352 with ratios obtained from *in-situ* measurements of soil erosion in Africa under similar environmental  
353 conditions (Dunne, 1979; Lal, 1985; El-Hassanin et al., 1993).

## 354 **4- Results**

### 355 *4.1 Model calibration with present-day in-situ data*

356 We first calibrated simulated water discharge to 114 years of monthly observed data available for  
357 Brazzaville/Kinshasa gauging station (1902-2016) (GRDC, 2016; HYBAM, 2016) (Fig. 6). A good  
358 correlation between the ranked monthly discharges observed and simulated by HydroTrend can be  
359 noticed (Fig. 6B), proving that HydroTrend is able to accurately simulate the Congo discharge at an  
360 annual scale, despite the large basin size and the heterogeneous climate of the catchment. The annual-  
361 averaged simulated discharge is  $41,650 \text{ m}^3 \text{ s}^{-1}$  and compares well with observations ( $41,480 \text{ m}^3 \text{ s}^{-1}$ ). At  
362 a monthly scale, simulated discharges match observed data for May to October, while the model  
363 underestimates by about 20% the discharges from November to January and overestimates discharges  
364 by about 20 % from February to April (Fig. 6C). These uncertainties may be due to difference of  
365 drainage area and/or morphology between the northern hemisphere ( $\sim 40 \%$  of the total drainage area,  
366 600 m of mean elevation) and the southern hemisphere ( $\sim 60 \%$  of the total drainage area, 800 m of  
367 mean elevation) parts of the catchment.

368 To calibrate SSL (Suspended Sediment Load), we used in-situ monitoring data at Brazzaville station,  
369 collected through several sources: preliminary survey in the 70s (Giresse and Moguedet, published in  
370 Kinga-Mouzeo, 1986), continuous once-a-month survey between 1987 and 1993 (PEGI program,  
371 Laraque et Orange, 1996) and continuous once-a-month survey from 2005 to present-day (HYBAM,

2016). Some complementary data are also available from Spencer et al., (2016). To compare observed and simulated data we simulated 20 years of daily sediment discharge. First, a simulation of SSL without any trapping shows a large discordance between observed and simulated data (Fig. 7A). Then, we added a classic trapping, that would most likely occurs in the low-slope lands of the Cuvette Centrale, which could be interpreted similarly as trapping in a lake. Simulation shows that this kind of trapping is not sufficient to match *in-situ* data, especially during high-discharge events (Fig. 7B). To adjust for these high-discharge events, we considered an additional trapping, within the wetlands of the floodplain. This kind of trapping concerns only sediments exported above bankfull discharges, that correspond to the discharge needed to flood the alluvial plain. Calibrating to the simulations, we get the best results when bankfull discharge is  $33,000 \text{ m}^3 \text{ s}^{-1}$ . This is about 20% lower than bankfull discharge calculated from empirical equations (Andreadis et al., 2013), and particularly low in comparison with mean annual discharge because some parts of the alluvial plains are almost permanently flooded. After taking this wetland trapping into account, simulated sediment load data match the observed data well (Fig. 7C). The mean SSL is respectively of  $1072 \text{ kg s}^{-1}$  for simulated data and  $974 \text{ kg s}^{-1}$  for *in-situ* data. This difference can be explained by the lack of *in-situ* measurements during very high-discharge events ( $> 65,000 \text{ m}^3 \text{ s}^{-1}$ ) that can lead to an underestimation of SSL. This underestimation is common as reliable sediment concentration measurements during high-discharge events are almost impossible to measure (e.g. Syvitski et al., 2003).

#### 4.2 Simulations of the last 155 ka.

Fig. 8A and B show the 500-year running averages of mean annual simulated sediment and water discharge leaving the Congo catchment over the last 155 ka. A change in water discharge correlated with climatic periods can be observed, with a mean discharge ranging from  $40,000$  to  $50,000 \text{ m}^3 \text{ s}^{-1}$  during warm stages (MIS 1, 5a, 5c, 5e) and around  $35,000 \text{ m}^3 \text{ s}^{-1}$  during main cold stages (MIS 2, 4, 6) (Fig. 8). Changes in water discharge are often drastic during transitional periods. Sediment discharge (Fig. 8) fluctuates more frequently. The minimum and maximum values (in grey Fig. 8) are calculated with respect to assumptions about the vegetation index (see part 3.3.2). The mean SSL curve (in black Fig. 8) overall indicates a negative correlation between water discharge and suspended sediment load. Differences between lower (in warm periods) and higher (in cold periods) sediment discharges can reach up to 50%, from  $950$  to  $1500 \text{ kg s}^{-1}$ . A focus on water and sediment discharges leaving the Congo catchment since the last 23 ka with a higher resolution is presented in Fig. 9. It aims to improve constrains on inter-annual variability and better understand the transitions between warm and cold periods. As already shown for the 155 ka simulation, mean annual water discharge (in black Fig. 9A) is about 25% less during the LGM. The inter-annual variation (in gray Fig. 9A) is also less during the LGM (15% compared to 30% today). Mean annual SSL varies between  $700$  and  $1900 \text{ kg s}^{-1}$  over the last 23 ka period (Fig. 9C), but the mean SSL averaged on a running mean over 100 years shows variations between  $950$  to  $1300 \text{ kg s}^{-1}$ , with an overall average of about  $1100 \text{ kg s}^{-1}$  (in black Fig. 9D).

408 The inter-annual discharge variability is not significantly different between LGM and present-day and  
409 the mean annual SSL is only about 10% higher during the LGM (in gray Fig. 9D). The highest SSL  
410 corresponds to a post-glacial period (16-12 ka) and a short event around 5-6 ka (further discussed in  
411 section 5.1). Two simulations, respectively without and with vegetation changes were performed (Fig.  
412 9B and 9C). They aimed to highlight the importance of vegetation changes, which largely guide  
413 second order variations and are responsible for the two high sediment periods previously mentioned. A  
414 20 year daily simulation that considers LGM environmental conditions (21 ka) was also performed in  
415 order to compare SSL between glacial and interglacial (present-day) periods (Fig. 10A). During LGM,  
416 the water discharge is lower, but because of the less dense vegetation cover, the concentration of  
417 sediment is higher. It results in a slightly higher SSL during LGM, and showing an increase of about  
418 15% ( $1221 \text{ kg s}^{-1}$  at LGM versus  $1072 \text{ kg s}^{-1}$  today). These results suggest that during cold periods, the  
419 climatic conditions are theoretically less favorable to the production of sediment, notably because of  
420 the lower precipitation rate. But at the same time, the regression of rainforests enhanced soil erosion  
421 and thus sediment production. Therefore, the two effects have opposite consequences on sediment  
422 production. Graphs of Fig. 10B and Fig. 10C aim to decipher the relative contribution of climate  
423 conditions (temperature and precipitation) (red curve) and vegetation cover (green curve) with respect  
424 to mean sediment load (black curve). Data are normalized for comparison with present-day. Except  
425 during warm periods (MIS 1, 5c and 5e), climate factors typically cause a decrease in sediment  
426 production in comparison to present-day. Decreases of forested land during colder periods enhanced  
427 sediment production. This explains why the sediment load varies only by 10-15% during most of the  
428 last 155 ka (except for some relatively short periods), while variations in climate conditions and  
429 vegetation cover could impact up to 30% the sediment load between the more and the less favorable  
430 periods (Fig. 10C). It also implies that peaks in sediment supply most likely occur when climate  
431 begins to warm, after a cooling period but vegetation had no chance yet to fully recover and reconquer  
432 the catchment, i.e. during post-glacial periods. In the case of the last deglaciation (16-12 ka) this peak  
433 reached about  $1300 \text{ kg s}^{-1}$ , i.e. 20 % higher than what is currently observed.

434 By extrapolating the period to 155 ka, highest simulated SSL peaks occurred during the MIS 5, with  
435 about 30 % more sediment than currently observed, and when climate changes were very rapid and  
436 intensive, between the cold (MIS 5b and 5d) and the warm (MIS 5a, 5c, 5e) inter-stages.

437

## 438 ***5- Discussion***

### 439 *5.1 Importance of vegetation cover changes*

440 Simulation results suggest there is a stronger control of vegetation cover on sediment load for the  
441 Congo catchment over precipitation and temperatures. Vegetation cover partly protects soil from

442 eroding by intercepting raindrops, enhancing infiltration, transpiring soil water, and increasing surface  
443 roughness (Rogers and Schumm, 1991; Castillo et al., 1997; Gyssels et al., 2005; Roller et al., 2012,  
444 El Kateb et al., 2013). In tropical zones the vegetation cover is strongly controlled by climatic  
445 conditions (Elenga et al., 2004; Dalibard et al., 2014). The sea surface temperature controls upwelling  
446 and monsoon intensity (Maley et al., 1997) and directly impacts tropical rainforest development.  
447 During the LGM, tropical rainforests decreased by about 70-80 % for the Congo catchment (Jolly et  
448 al., 1998; Rommerkirchen et al., 2006). Simulations suggest that this decrease in rainforest could be  
449 responsible for enhancing sediment production by more than 30 %, while external climatic variations  
450 account only for a 20 % decrease in sediment during glacial stages. A peak of sediment load occurred  
451 at around 5 ka (Fig. 9D). This sediment peak reflects a decrease in rainforest coverage during a period  
452 when no change in climatic condition is detected (Fig. 10B) (Bayon et al., 2012; Dalibard et al., 2014).  
453 This event, probably more accurately dated by pollen studies onshore at 3 ka (e.g. Elenga et al., 2004)  
454 instead of the 5 ka that was dated by offshore proxies, was associated to a global intensification of  
455 erosional processes (Maley, 1992; Bayon et al., 2012). It was interpreted as resulting from a potential  
456 change in rainfall variability, due to the setting of convective atmospheric systems leading to an  
457 alternation between dry periods and very strong precipitation events responsible for an increase of  
458 runoff and a decrease of water infiltration (Maley, 1982; Maley et al., 2000). The presence of human  
459 activities in the forest at this time, evidenced by archeological studies (Wotzka 2006; Brncic et al.  
460 2007; Morin-Rivat et al., 2014) could also be a forcing factor, limiting forest development, as  
461 suggested by Bayon et al. (2012), although the specific role of human impact is still largely questioned  
462 (Neumann et al., 2012; Maley et al., 2012).

463 *5.2 Mass budget comparison between exported sediments, denudation and weathering rates*  
464 *and sediments deposited offshore.*

465 Present-day specific sediment load exported from the Congo catchment, estimated from the most  
466 recent river load compilation (Laraque et al., 2013b) is  $2,725 \text{ kg s}^{-1}$  ( $1,046 \text{ kg s}^{-1}$  of TSS and  $1,679 \text{ kg}$   
467  $\text{s}^{-1}$  of dissolved matter). This corresponds to an erosion rate of about  $23 \text{ t km}^{-2} \text{ yr}^{-1}$ , consistent with the  
468  $19 \text{ t km}^{-2} \text{ yr}^{-1}$  indicated by previous studies (NKounkou and Probst, 1987; Summerfield and Hulton,  
469 1994). Present-day global mass budget deduced from geochemical analyses is  $13 \text{ t km}^{-2} \text{ yr}^{-1}$  (Gaillardet  
470 et al., 1995). Different estimates are therefore of the same order of magnitude. At longer timescales  
471 ( $10^5$ - $10^6$  years), our results suggest denudation rates of about  $26 \text{ t km}^2 \text{ yr}^{-1}$ , considering a constant ratio  
472 between suspended and dissolved sediment load. Denudation rates deduced from cosmogenic studies  
473 suggest a similar rate of about  $27 \text{ t km}^2 \text{ yr}^{-1}$  for the Congo basin (Al-Gharib, 1992), which is in the  
474 same range as other cosmogenic studies for drainage basins in central and western Africa, located in  
475 similar climatic, morphologic and lithologic setting. For example, 8 to  $22 \text{ t km}^{-2} \text{ yr}^{-1}$  for the Burkina-  
476 Faso craton (Brown et al., 1994) and 7 to  $16 \text{ t km}^{-2} \text{ yr}^{-1}$  for the Nyong River in Cameroon (Regard et  
477 al., 2016). These estimates are stable over long geological timescales ( $10^7$ - $10^8$  years), since mass

478 budgets determined from morphological studies suggest rates of  $14.6 \text{ t km}^{-2} \text{ yr}^{-1}$  (Guillocheau et al.,  
479 2016) to  $16\text{-}22 \text{ t km}^{-2} \text{ yr}^{-1}$  over the last 35 Ma (Leturmy et al., 2003), in the same range as other but  
480 similar catchments in central and western Africa (Beauvais and Chardon, 2013). This good agreement  
481 between modern and long-term sediment fluxes was also evidenced in similar settings (lowland areas  
482 of large catchments), such as the Amazon (Wittmann et al., 2011) but also for landscapes considered  
483 in equilibrium (Clapp et al., 2001; Matmon et al., 2003; Vance et al., 2003). Offshore the Congo, most  
484 of the sediments are deposited within the deep-sea fan (Droz et al., 2003; Savoye et al., 2009) since the  
485 outlet of the watershed is connected to the deep canyon indifferently during high or low eustatic stages  
486 (Babonneau et al., 2002). Volumes of sediment deposited in the most recent turbidite fan (axial fan)  
487 were accurately estimated for several cycles of sedimentation over the last 210 ka (Picot, 2015; Picot  
488 et al., 2016). The periods concerned are 0-11 ka; 11-75 ka; 75-130 ka; 130-210 ka. Decompacted  
489 volumes given by Picot (2015) were transformed into mass using a density of  $1.8 \text{ t m}^{-3}$ , allowing for  
490 comparison to simulated riverine sediment loads. These volumes can be compared to budgets deduced  
491 from our sediment load results since more than 95 % of sediment preserved in the deep-sea fan is  
492 provided by the Congo River (Gingele et al., 1998). The total decompacted volume of sediment of the  
493 axial fan is about  $8,500 \text{ km}^3$  (Picot et al., 2016) recently re-evaluated to  $7,700 \text{ km}^3$  (Laurent et al.,  
494 2017), which corresponds to an equivalent erosion rate of  $18.8 \pm 0.9 \text{ t km}^{-2} \text{ yr}^{-1}$  or a mean sediment  
495 load of about  $2200 \pm 100 \text{ kg s}^{-1}$ . These sediment loads are of the same order of magnitude as the  
496 previously published erosion rates, determined using different independent methods (Al-Gharib, 1992;  
497 Gaillardet et al., 1995; Leturmy et al., 2003; Guillocheau et al., 2016). This indicates that a large part  
498 of exported matter, including dissolved matter, is preserved in the sediment of the deep-sea fan. Two  
499 thirds of the matter exported from the Congo catchment is dissolved (Laraque et al., 2013b), but the  
500 biogenic part of marine sediments represents less than 30 % of the turbidite fan sedimentation. This  
501 biogenic part consists mainly of siliceous biogenic sediments (Schneider et al., 1997, Hatin et al.,  
502 2017). For the Amazon, biogenic silica is formed as soon as the dissolved load comes in contact with  
503 the marine domain, because of the change in redox conditions, but this biogenic silica also very  
504 rapidly weathers into authigenic K-Fe-rich aluminosilicates (Michalopoulos and Aller, 2004). K-Fe-  
505 rich aluminosilicates are present in the Congo sedimentary system (Giresse et al., 1988; Amouric et  
506 al., 1994) suggesting that the same kind of processes may occur for the Congo dissolved matter. The  
507 rapid recycling of biogenic silica to authigenic clays might explain why the biogenic part in marine  
508 sediments is much lower than dissolved matter exported from the catchment.

509 In detail, decompacted volumes estimated from Laurent et al. (2017) are:  $992 \text{ km}^3$  for the 0-11 ka  
510 period, i.e.  $43.9 \text{ t km}^{-2} \text{ yr}^{-1}$ ;  $3,730 \text{ km}^3$  for the 11-75 ka period, i.e.  $28.4 \text{ t km}^{-2} \text{ yr}^{-1}$ ;  $904 \text{ km}^3$  for the 75-  
511 130 ka period, i.e.  $8 \text{ t km}^{-2} \text{ yr}^{-1}$  and  $2,073 \text{ km}^3$  for the 130-210 ka period, i.e.  $12.6 \text{ t km}^{-2} \text{ yr}^{-1}$ . The  
512 period 0-75 ka presents a corresponding sediment load about three times higher than for the period 75-  
513 210 ka, which is not consistent with results of the sediment load simulations. The simulations do not

514 suggest a significant difference of sediment inputs between these two periods (1,151 kg s<sup>-1</sup> for 0-75 ka;  
515 1,173 kg s<sup>-1</sup> for 75-155 ka). A remobilization of older sediments in the most recent deposits might  
516 explain this difference but the good stacking and preservation of turbidite features over the last 800 ka  
517 (Droz et al., 2003; Marsset et al., 2009) argues against this assumption. Another possible explanation  
518 is that very large catchments such as the Congo may buffer high-frequency oscillations (Métivier and  
519 Gaudemer, 1999; Castelltort and Van den Driessche, 2003) by the more or less temporary storage of  
520 sediments on the alluvial plain (Wittmann et al., 2011). Indeed, large pulses of mobile sediment may  
521 be buffered if the amount of sediment stored in a floodplain is large relative to the sediment load.  
522 Similar, the stream may maintain an important load of sediment when hinterland sediment production  
523 is reduced, due to the presence of transportable debris stored in the floodplain (Phillips, 2003). The  
524 agreement of modern and long-term output fluxes of the Congo could thus be explained by this  
525 buffering capacity of the floodplain and/or of the estuary (Eisma and Kalf, 1984), while sediment  
526 loads deduced from our simulations and those deduced from stratigraphic records may mismatch over  
527 shorter wavelength (< 10<sup>5</sup> yrs) due to the same buffering effect, as demonstrated by Castelltort and  
528 Van den Driessche (2003) and Simpson and Castelltort (2012) for large watersheds. In similar studies,  
529 the size of the catchment has also been already evoked as a parameter allowing for the buffering of  
530 water and sediment discharges over a glacial/interglacial cycle (Kettner and Syvitski, 2009). Note also  
531 that only suspended sediment load is simulated here, dissolved matter and bedload might have a  
532 different behavior with respect to trapping and release in the catchment and thus could also contribute  
533 to explain a mismatch between sediment exportation and stratigraphic records over short wavelength.

### 534 *5.3 Simulation comparison with chemical proxies deduced from marine cores*

535 Numerous oceanographic cruises were conducted in the study area during the last decades (Cochonat  
536 and Robin, 1992; Cochonat, 1998; Savoye, 1998; Marsset and Droz, 2010; Droz and Marsset, 2011).  
537 These cruises allowed for a detailed, comprehensive offshore dataset which led to many environmental  
538 studies that aimed to better understand regional paleo-environmental conditions and their implications  
539 in term of source-to sink water and sediment budgets and continental weathering over a certain period  
540 (e.g. Bayon et al., 2012; Dalibard et al., 2014; Picot et al., 2016; Hardy et al., 2016; Hatin et al., 2017).  
541 From these studies, we retain the main classically used proxies in relation to water and sediment  
542 transport capacity and intensity of weathering for comparisons with water and sediment supply  
543 determined from the here presented model simulations. Note that due to the large size of the catchment  
544 and its ability to buffer small wave-length variations in environmental conditions, chemical proxies  
545 extracted from marine cores may only approximately represent continental conditions and should be  
546 used with caution. Most of the data used were obtained from core KZai-02 drilled during ZaiAngo1  
547 cruise (Savoye et al., 1998).



548 The chemical erosion of silicates (i.e. weathering) is defined by the alteration of K-feldspar to  
549 kaolinite. A high Al/K ratio reflects a high abundance of kaolinite and thus a high weathering degree  
550 (e.g. Schneider et al., 1997). We thus used an Al/K semi-quantitative ratio measured with a XRF core  
551 scanner for core KZai-02 (Hatin et al., 2017). For core KZai-01, located very close to KZai-02 (Fig.  
552 1), it was shown that quantitative measurements of Al/K (Bayon et al., 2012) follow a similar trend as  
553 semi-quantitative ratios (Picot, 2015), allowing for the interpretation of semi-quantitative values as  
554 representative of weathering intensity. Al/K ratio (Fig. 11C) is lower during cold periods indicating a  
555 less efficient chemical weathering consistent with a lower water runoff (Fig. 11B) especially during  
556 MIS2, MIS4 and MIS5b. At the same time sediment load increases (Fig. 11A) during cold stages,  
557 meaning that physical erosion processes get enhanced in comparison with chemical processes. The  
558 kaolinite/smectite ratio also reflects the weathering degree (Gingele et al., 1998). The  
559 kaolinite/smectite ratio measured for KZai-02 (Sionneau et al., 2010) (Fig. 11D) follows a trend  
560 similar to Al/K ratio but is less clear, since this ratio responds over a large timescale and is very  
561 sensitive to the sediment source (Thiry, 2000). Ti/Ca ratio is a tracer of fluvial intensity since titanium  
562 is an immobile element in coarse sediment, while calcium resides in easily dissolvable minerals (e.g.  
563 Adegbie et al., 2003; Govin et al., 2012). For the Congo, high values of Ti/Ca (Fig. 11E) only  
564 occurred during long humid phases (MIS5e and MIS1) and thus do not systematically correlate with  
565 water discharge (Fig. 11B). Short wave-length variations of water discharge are probably buffered by  
566 trapping capability in the catchment (see discussion in section 5.1) and explain why the Ti/Ca ratio  
567 does not accurately reflect the fluvial variation of the Congo. We also computed total organic carbon  
568 (TOC) for core KZai-02 (Picot, 2015) since it correlates well with climate cycles (Fig. 11F). We  
569 observe an increase from 1% to 2-3% of TOC during cold periods. Most of this organic carbon has a  
570 continental origin for recent periods (late Holocene) (Baudin et al., 2010), but the increase of TOC  
571 during glacial stages is not consistent with the decrease in vegetation cover at that same period.  
572 Schneider et al. (1997) deciphered continental and marine organic carbon in the Congo's marine  
573 sediments over the last 200 ka and demonstrated that terrestrial organic carbon did not fluctuate  
574 significantly in time, while fluctuations in TOC over glacial/interglacial stages are mainly controlled  
575 by marine organic carbon. During cold periods, primary productivity might be enhanced by strong  
576 trade winds which could reinforce upwelling and change thermoclines (Schneider et al., 1997; Berger  
577 et al., 2002). The TOC seems thus controlled by the marine organic carbon rate, that is higher during  
578 glacial stages while terrestrial conditions are less favorable for the development of vegetation and  
579 exportation of organic carbon from the continent (less runoff and more sediment exported, Fig. 11B  
580 and C).

## 581 **6- Conclusions**

582 We numerically simulated water and sediment supply exported to the ocean by the Congo, the second  
583 largest river in the world in terms of discharge and drainage area, over the last 155 ka. This work is a  
584 first attempt to use the numerical model HydroTrend on such a long time scale and on such a large  
585 catchment. In context of the Congo, climate and land cover changes are the main drivers controlling  
586 water and sediment supply to the ocean. For this study, numerous calibrating datasets existed over  
587 long time scales, allowing for accurate long-term simulations ( $>10^5$  years). Despite the size of the  
588 watershed, HydroTrend was able to accurately simulate water discharge and sediment load exported  
589 from the Congo. Climate and land cover changes were calibrated using global climate models, marine  
590 proxies and remote sensing data. In particular, we developed an original approach for quantifying the  
591 impact of vegetation changes. Results show that water discharge is very sensitive to climate, with a  
592 decrease in discharge of about 25% during glacial stages. Sediment load is more sensitive to  
593 vegetation changes than climate changes themselves. Variations in sediment load can reach up to more  
594 than 30% in comparison with present-day during periods when climate began to warm and vegetation  
595 did not have the chance yet to grow and extend again, i.e. during post-glacial stages. Overall, despite a  
596 decrease in water discharge, the loss of rainforest enhanced soil erosion and thus sediment load  
597 slightly increased during glacial stages. We also highlight that trapping is important in the catchment  
598 and occurred in the wetlands and flood plains of the lowlands. This trapping act as a buffer for small  
599 wave-length environmental variations, making interpretations in a source-to-sink approach more  
600 challenging, from a stratigraphic, sedimentologic and chemical point of view. In future, our approach  
601 and the novelties we added to HydroTrend could be applied for other large tropical catchments of e.g.  
602 Africa, in order to infer the potential effect of environmental changes on water and sediment  
603 discharge.

## 604 ***7- Acknowledgements***

605 This work benefited from a State Grant from the French "Agence Nationale de la Recherche (ANR)"  
606 in the Program "Investissements d'Avenir" (ANR-10-LABX-19-01, Labex Mer). USA co-author AK  
607 was supported through the NSF continuing Grant 0621695. We are grateful to the two anonymous  
608 reviewers for their fruitful comments which contributed to improve the manuscript. We thank M.  
609 Picot, G. Bayon and N. Freslon for fruitful discussions. The work also benefited from data acquired  
610 during oceanographic cruises (Guiness and ZaiAngo).

611

## 612 ***References cited***

613 Adegbe, A.T., Schneider, R.R., Röhl, U., Wefer, G., 2003. Glacial millennial-scale fluctuations in central  
614 African precipitation recorded in terrigenous sediment supply and freshwater signals offshore Cameroon.  
615 *Palaeogeogr., Palaeoclimatol., Palaeoecol.* 197(3–4), 323–333, doi:10.1016/S0031-0182(03)00474-7

616 Algharib, I., 1992. Apport des isotopes à vie moyenne de l'Uranium et du Thorium,  $^{210}\text{Pb}$  et  $^{10}\text{Be}$  dans l'étude  
617 de l'érosion chimique et physique de deux grands bassins: Amazone et Congo. PhD thesis, Univ. Nice-  
618 Sophia Antipolis.

619 Alsdorf, D., Beighley, E., Laraque, A., Lee, H., Tshimanga, R., O'Loughlin, F., Mahé, G., Dinga, B., Moukandi  
620 G., Spencer, R.G.M., 2016. Opportunities for hydrologic research in the Congo Basin. *Reviews of*  
621 *Geophysics* 54, doi:10.1002/2016RG000517.

622 Amouric, M., Parron, M., Casalini, C., Giresse, P., 1995. A (1: 1) 7-Å Fe phase and its transformation in recent  
623 sediments: An HRTEM and AEM study. *Clays and Clay Min.* 43, 446–454.

624 Andreadis, K.A., Schumann, G. J.-P., Pavelsky, T., 2013. A simple global river bankfull width and depth  
625 database. *Water Resour. Res.* 49, 7164–7168, doi:10.1002/wrcr.20440.

626 Babonneau, N., Savoye, B., Cremer, M., Klein, B., 2002. Morphology and architecture of the present canyon and  
627 channel system of the Zaire deep-sea fan. *Mar. Pet. Geol.* 19, 445–467. doi:10.1016/S0264-  
628 8172(02)00009-0

629 Barnes, R.F.W., 1990. Deforestation trends in tropical Africa. *African Journal of Ecology* 28, 161-173.

630 Baudin, F., Disnar, J.-R., Martinez, P., Dennielou, B., 2010. Distribution of the organic matter in the channel-  
631 levees systems of mud-rich deep-sea fan (West Africa). Implication for deep offshore source rocks and  
632 global carbon cycle. *Marine and Petroleum Geology* 27, 995-1010.

633 Bayon, G., Dennielou, B., Etoubleau, J., Ponzevera, E., Toucanne, S., Bermell, S., 2012a. Intensifying  
634 Weathering and Land Use in Iron Age Central Africa. *Science* 335, 1219–1222.  
635 doi:10.1126/science.1215400

636 Bear, J. 1972. Dynamics of fluids in porous media. Courier corporation, 764 pp.

637 Beauvais, A., Chardon, D., 2013. Modes, tempo, and spatial variability of Cenezoic cartonic denudation : The  
638 West Afracan example. *Geochemistry, Geophysics, Geosystems* 14, doi:10.1002/ggge.20093

639 Becker, M., Santos da Silva, J., Calmant, S., Robinet, V., Linguet, L., Seyler, F., 2014. Water Level Fluctuations  
640 in the Congo Basin Derived from ENVISAT Satellite Altimetry. *Remote Sensing* 6, 9340-9358.  
641 doi:10.3390/rs6109340

642 Beighley, R.E., Ray, R.L., He, Y., Lee, H., Schaller, L., Andreadis, K.M., Durand, M., Alsdorf, D.E., Shum,  
643 C.K., 2011. Comparing satellite derived precipitation datasets using the Hillslope River Routing (HRR)  
644 model in the Congo River Basin. *Hydrological Processes* 25, 3216–3229. doi:10.1002/hyp.8045.

645 Berger, W.H., Lange, C.B., Wefer, G., 2002. Upwelling history of the Benguela-Namibia system: a synthesis of  
646 Leg 175 results. In Wefer, G., Berger, W.H., Richter, C. (Eds.), *Proc. ODP, Sci. Results* 175, 1–103.

647 Boyer, J.-F., Dieulin, C., Rouche, N., Cres, A., Servat, E., Paturel, J.-E., Mahé, G., 2006. SIEREM an  
648 environmental information system for water resources. 5th World FRIEND Conference, La Havana -  
649 Cuba, November 2006 in *Climate Variability and Change – Hydrological Impacts IAHS Publ.* 308, 9-25.

650 Brncic, T.M., Willis, M.K.J., Harris, D.J., Washington, R., 2007. Culture or climate? The relative influences of  
651 past processes on the composition of the lowland Congo rainforest. *Philosophical Transactions of the*  
652 *Royal Society of London B* 362(1478), 229–242.

653 Brown, E.T., Boulès, D.L., Colin, F., Sanfo, Z., Raisbeck, G.M., Yiou, Y., 1994. The development of iron crust  
654 lateritic system in Burkina Faso, West Africa, examined with in-situ produced cosmogenic nuclides.  
655 *Earth Planet. Sci. Lett.* 124, 19 – 33.

656 Bruijnzeel, L.A., 2004. Hydrological functions of tropical forests: not seeing the soil for the trees? *Agriculture,*  
657 *Ecosystems and Environment* 104, 185-228.

658 Brune, G.M., 1953. Trap efficiency of reservoirs. *Trans Am Geophys Union* 34, 407–418.

659 Bultot, F., 1972. Atlas Climatique du Bassin Congolais. Publications de L'Institut National pour L'Etude  
660 Agronomique du Congo (I.N.E.A.C.), 3° Partie, Température et Humidité de L'Air, Rosee, Température  
661 du Sol.

662 Caley, T., Malaizé, B., Revel, M., Ducassou, E., Wainer, K., Ibrahim, M., Shoeaib, D., Migeon, S., Marieu, V.,  
663 2011. Orbital timing of the Indian, East Asian and African boreal monsoons and the concept of a “global  
664 monsoon.” *Quat. Sci. Rev.* 30, 3705–3715. doi:10.1016/j.quascirev.2011.09.015

665 Castelltort, S., Van Den Driessche, J., 2003. How plausible are high-frequency sediment supply-driven cycles in  
666 the stratigraphic record? *Sedimentary Geology* 157, 3–13, doi:10.1016/S0037-0738(03)00066-6.

- 667 Castillo, V.M., Martinez-Mena, M., Albaladejo, J., 1997. Runoff and soil loss response to vegetation removal in  
668 a semiarid environment. *Soil Sci. Soc. Am. J.* 61, 1116 – 1121,  
669 doi:10.2136/sssaj1997.03615995006100040018x.
- 670 Clapp, E.M., Bierman, P.R., Nichols, K.K., Pavich, M., Caffee, M., 2001. Rates of sediment supply to arroyos  
671 from upland erosion determined using in situ produced cosmogenic <sup>10</sup>Be and <sup>26</sup>Al. *Quaternary Research*  
672 55, 235–245.
- 673 Cochonot, P., 1998. ZAIANGO2 cruise, L'Atalante R/V. doi:10.17600/98010110
- 674 Cochonot, P., Robin, A., 1992. GUINNESS I cruise, L'Atalante R/V. doi:10.17600/92004211
- 675 Coulter, G.W., 1991. *Lake Tanganyika and its life*. Oxford Univ. Press, New York.
- 676 Coynel, A., Seyler, P., Etcheber, H., Meybeck, M., Orange, D., 2005. Spatial and seasonal dynamics of total  
677 suspended sediment and organic carbon species in the Congo River. *Global biogeochemical cycles* 19,  
678 GB4019.
- 679 Crétaux, J.-F., Jelinski, W., Calmant, S., Kouraev, A., Vuglinski, V., Bergé-Nguyen, M., Gennero, M.-C., Nino,  
680 F., Abarca Del Rio, R., Cazenave, A., Maisongrande, P., 2011. SOLS: A lake database to monitor in the  
681 Near Real Time water level and storage variations from remote sensing data. *Advance in Space Research*  
682 47, 1497-1507.
- 683 Crippen, R.E., 1990. Calculating the vegetation index faster, *Remote Sensing of Environment* 34, 71-73.
- 684 De Namur, C., 1990. Aperçu sur la végétation de l'Afrique Centrale Atlantique. in Lanfranchi R., Schwartz, D.  
685 (eds). *Paysages Quaternaires de l'Afrique Centrale Atlantique*, Inst. Fr. de Rech. Sci. pour le Dev. en  
686 Coop. (ORSTOM), Paris.
- 687 De Vente, J., Poesen, J., 2005. Predicting soil erosion and sediment yield at the basin scale: scale issues and  
688 semi-quantitative models. *Earth-Science Reviews* 71, 95-125.
- 689 Dalibard, M., Popescu, S.-M., Maley, J., Baudin, F., Melinte-Dobrinescu, M.-C., Pittet, B., Marsset, T.,  
690 Dennielou, B., Droz, L., Suc, J.-P., 2014. High-resolution vegetation history of West Africa during the  
691 last 145 ka. *Geobios* 47, 183–198. doi:10.1016/j.geobios.2014.06.002
- 692 Droz, L., Marsset, T., 2011. REPRESAI\_LEG2 cruise, Le Suroît R/V. doi:10.17600/11020020
- 693 Droz, L., Marsset, T., Ondréas, H., Lopez, M., Savoye, B., Spy-Anderson, F.-L., 2003. Architecture of an active  
694 mud-rich turbidite system: The Zaire Fan (Congo–Angola margin southeast Atlantic). *Results from*  
695 *ZaiAngo 1 and 2 cruises*. *AAPG Bull.* 87, 1145–1168. doi:10.1306/03070300013
- 696 Dunne, T., 1979. Sediment yield and land use in tropical catchments. *Journal of Hydrology* 42, 281-300.
- 697 Elenga, H., Maley, J., Vincens, A., Farrera, I., 2004. Palaeoenvironments, Palaeoclimates and Landscape  
698 development in Atlantic equatorial Africa: a review of key sites covering the last 25 kyrs. In Battarbee  
699 R.W. et al. (eds), *Past Climate Variability through Europe and Africa*. Kluwer Academic Publishers,  
700 Dordrecht, The Netherlands, 181-198.
- 701 El-Hassanin, A.S., Labib, T.M., Gaber, E.I., 1993. Effect of vegetation cover and land slope on runoff and soil  
702 losses from the watersheds of Burundi. *Agriculture, Ecosystems and Environment* 43, 301-308.
- 703 El Kateb, H., Zhang, H., Zhang, P., Mosandl, R., 2013. Soil erosion and surface runoff on different vegetation  
704 covers and slope gradients: a field experiment in Southern Shaanxi Province, China. *Catena* 105, 1-10.
- 705 Ellis, E.E., Keil, R.G., Ingalls, A.E., Richey, J.E., Alin, S.R., 2012. Seasonal variability in the sources of  
706 particulate organic matter of the Mekong River as discerned by elemental and lignin analyses. *J.*  
707 *Geophys. Res.* 117, G01038, doi:10.1029/2011JG00.
- 708 Farr, T.G., Rosen, P.A., Caro, E., Crippen, R., Duren, R., Hensley, S., Kobrick, M., Paller, M., Rodriguez, E.,  
709 Roth, L., Seal, D., Shaffer, S., Shimada, J., Umland, J., Werner, M., Oskin, M., Burbank, D.W., Alsdorf,  
710 D., 2007. The Shuttle radar topography mission. *Reviews of Geophysics* 45, RG2004.
- 711 Flügel, T.J., Eckardt, F.D., Cotterill, F.P.D., 2015. The present day drainage patterns of the Congo river system  
712 and their Neogene evolution. in: M.J. de Wit et al. (eds.), *Geology and Resource Potential of the Congo*  
713 *Basin, Regional Geology Reviews*, Springer-Verlag Berlin Heidelberg. DOI 10.1007/978-3-642-29482-  
714 2\_15
- 715 Gaillardet, J., Dupré, B., Allègre, C.J., 1995. A global chemical budget applied to the Congo basin rivers:  
716 Erosion rates and continental crust composition, *Geochim. Cosmochim. Acta* 59, 3469 – 3485.
- 717 Gent, P.R., Danabasoglu, G., Donner, L.J., Holland, M.M., Hunke, E.C., Jayne, S.R., Lawrence, D.M., Neale,  
718 I.B., Rasch, P.J., Vertenstein, M., Worley, P.H., Yang, Z.-L., Zhang, M., 2011. The Community Climate  
719 System Model Version 4. *Journal of Climate* 24, 4973-4991.

720 Gingele, F.X., Müller, P.M., Schneider, R.R., 1998. Orbital forcing of freshwater input in the Zaire Fan area -  
721 clay mineral evidence from the last 200 kyr. *Palaeogeogr. Palaeoclimatol. Palaeoecol.* 138, 17–26.  
722 doi:10.1016/S0031-0182(97)00121-1

723 Giresse, P., Wiewiora, A., Lacka, B., 1988. Mineral phases and processes within green peloids from two recent  
724 deposits near the Congo River mouth. *Clay Minerals* 23, 447–458.

725 GRDC, Global Runoff Data Center, 2016. [http://www.bafg.de/GRDC/EN/Home/homepage\\_node.html](http://www.bafg.de/GRDC/EN/Home/homepage_node.html) (last  
726 accessed October 2016).

727 Govin, A., Holzwarth, U., Heslop, D., Ford Keeling, L., Zabel, M., Mulitza, S., Collins, J.A., Chiessi, C.M.,  
728 2012. Distribution of major elements in Atlantic surface sediments (36°N–49°S): Imprint of terrigenous  
729 input and continental weathering. *Geochem. Geophys. Geosystems* 13, Q01013.  
730 doi:10.1029/2011GC003785

731 Guillocheau, F., Chelalou, R., Linol, B., Dauteuil, O., Robin, C., Mvondo, F., Callec, Y., Colin, J.-P., 2015.  
732 Cenozoic Landscape Evolution in and Around the Congo Basin: Constraints from Sediments and  
733 Planation Surfaces. in: M.J. de Wit et al. (eds.), *Geology and Resource Potential of the Congo Basin*,  
734 *Regional Geology Reviews*, Springer-Verlag Berlin Heidelberg. DOI 10.1007/978-3-642-29482-2\_14

735 Guillocheau, F., Galmier, V., Robin, C., 2016. Source to Sink study of the Congo system since 40 Myr: a  
736 measurement ratio between mechanical and chemical erosion. *In* “Source to Sink: a long term perspective  
737 of sediment budgets and sources characterization” meeting, Nov 2016, Rennes, France. Abstracts book,  
738 p.62.

739 Gyssels, G., Poesen, J., Bochet, E., Li, Y., 2005. Impact of plant roots on the resistance of soils to erosion by  
740 water: a review, *Prog. Phys. Geogr.*, 29(2), 189 – 217.

741 Hardy, W., Penaud, A., Marret, F., Bayon, G., Marsset, T., Droz, L., 2016. Dinocyst assemblage constraints on  
742 oceanographic and atmospheric processes in the eastern equatorial Atlantic over the last 44 kyr.  
743 *Biogeosciences* 13, 4823–4841. <http://dx.doi.org/10.5194/bg-13-4823-2016>.

744 Hatin, T., Crosta, X., Le Hérisse, A., Droz, L., Marsset, T., 2017. Diatom response to oceanographic and climatic  
745 changes in the Congo fan area, equatorial Atlantic Ocean, during the last 190 ka BP. *Palaeogeogr.,*  
746 *Palaeoclimatol., Palaeoecol.* 469, 47-59.

747 Hijmans, R.J., Cameron, S.E., Parra, J.L., Jones, P.G., Jarvis, A., 2005. Very high resolution interpolated climate  
748 surfaces for global land areas. *International Journal of Climatology* 25, 1965–1978.

749 Huete, A., Disan, K., Miura, T., Rodriguez, E.P., Gao, X., Ferreira, L.G., 2002. Overview of the radiometric and  
750 biophysical performance of the MODIS vegetation indices. *Remote Sensing of Environment* 83, 195-213.

751 HYBAM, 2016. Contrôles géodynamique, hydrologique et biogéochimique de l'érosion/altération et des  
752 transferts de matière dans les bassins de l'Amazonie, de l'Orénoque et du Congo. Available at  
753 <http://www.ore-hybam.org>, (last accessed Nov. 2016).

754 Jolly, D., Harrison, S.P., Dammati, B., Bonnefille, R., 1998. Simulated climate and biomes of Africa during the  
755 Quaternary: comparison with pollen and Lake Status data. *Quaternary Science Reviews* 17, 629-657.

756 Jung, H.K., Hamski, J., Durand, M., Alsdorf, D., Hossain, F., Lee, H., Azad Hossain, A.K.M., Hasan, K., Saleh  
757 A., Khan, Zeaul Hoque, A.K.M., 2010. Characterization of complex fluvial systems using remote sensing  
758 of spatial and temporal water level variations in the Amazon, Congo, and Brahmaputra Rivers, *Earth*  
759 *Surface Processes and Landforms* 35, 294 –304, doi:10.1002/esp.1914.

760 Kettner, A.J., Syvitski, J.P.M., 2008. HydroTrend v. 3.0: A climate-driven hydrological transport model that  
761 simulates discharge and sediment load leaving a river system. *Computers & Geosciences* 34 (10), 1170-  
762 1183.

763 Kettner, A.J., Syvitski, J.P.M., 2009. Fluvial responses to environmental perturbations in the Northern  
764 Mediterranean since the Last Glacial Maximum. *Quaternary Science Reviews* 28 (23), 2386-2397.

765 Kinga-Mouzeo, 1986. Transport particulaire actuel du fleuve Congo et de quelques affluents; enregistrement  
766 quaternaire dans l'éventail détritique profond (sédimentologie, minéralogie et géochimie). PhD thesis,  
767 Université de Perpignan. 251 pp.

768 Kottek, M., Grieser, J., Beck, C., Rudolf, B., Rubel, F., 2006. World Map of the Köppen-Geiger climate  
769 classification updated. *Meteorologische Zeitschrift* 15(3), 259-263.

770 Kutzbach, J., Gallimore, R., Harrison, S., Behling, P., Selin, R., Laarif, F., 1998. Climate and Biome simulations  
771 for the past 21,000 years. *Quaternary Science Reviews* 17, 473-506.

772 Lal, R., 1985. Soil erosion and sediment transport research in tropical Africa. *Hydrological Sciences Journal* 30  
773 (2), 239-256. DOI: 10.1080/02626668509490987

774 Laraque, A., Bricquet, J.P., Berthelot, M., Olivry, J.C., 1995. Aspects hydrologiques du fleuve Congo.  
775 Proceeding of PEGI international meeting 22-44 may 1993, CNRS-INSU-ORSTOM, Paris.

776 Laraque, A., Orange, D., 1996. Banque de données hydrochimiques des eaux de surfaces d’Afrique Centrale  
777 (Congo et Oubangui) de 1987 à 1994. Programme PEGI-GBF, ORSTOM, Montpellier. 145 pp.

778 Laraque, A., Pouyaud, B., Rocchia, R., Robin R., Chaffaut I., Moutsambote, J.-M., Maziezoula, B., Censier, C.,  
779 Albouy, Y., Elenga, H., Etcheber, H., Delaune, M., Sondag, F., Gasse, F., 1998. Origin and function of a  
780 closed depression in equatorial humid zones: the lake Tele in north Congo. *Journal of Hydrology* 207,  
781 236–253.

782 Laraque, A., Bricquet, J.P., Pandi, A., Olivry, J.C., 2009. A review of material transport by the Congo river and  
783 its tributaries. *Hydrological Processes* 23, 3216-3224.

784 Laraque, A., Bellanger, M., Adele, G., Guebanda, S., Gulemvuga, G., Pandi, A., Paturel, J.E., Robert, A., Tathy,  
785 J.P., Yambele A. 2013a. Evolutions récentes des débits du Congo, de l’Oubangui et de la Sangha. 2013a.  
786 *Geo-Eco-Trop.* 37(1), 93-100.

787 Laraque, A., Castellanos, B., Steiger, J., López, J.L., Pandi, A., Rodriguez, M., Rosales, J., Adèle, G., Perez, J.,  
788 Lagane, C., 2013b. A comparison of the suspended and dissolved matter dynamics of two large inter-  
789 tropical rivers draining into the Atlantic Ocean: the Congo and the Orinoco. *Hydrol. Process.* 27, 2153–  
790 2170. doi:10.1002/hyp.9776

791 Latham, J., Cumani, R., Rosati, I., Bloise, M., 2014. Global Land Cover SHARE (GLC-SHARE) database Beta-  
792 Release Version 1.0. Rome: FAO. Accessed March 27.  
793 [http://www.glc.org/downloads/prj/glcshare/GLC\\_SHARE\\_beta\\_v1.0\\_2014.pdf](http://www.glc.org/downloads/prj/glcshare/GLC_SHARE_beta_v1.0_2014.pdf)

794 Latrubesse, E.M., Arima, E.Y., Dunne, T., Park, E., Baker, V.R., d’Horta, F.M., Wight, C., Wittmann, F.,  
795 Zuanon, J., Baker, P.A., Ribas, C.C., Norgaard, R.B., Filizola, N., Ansar, A., Flyvbjerg B., and Stevaux  
796 J.C., 2017. Damming the rivers of the Amazon basin. *Nature* 546, 363–369 doi:10.1038/nature22333

797 Laurent D., Picot M., Marsset T., Droz L., Rabineau M., Granjeon D., Molliex S., 2017. 3D stratigraphic  
798 modeling of the Congo turbidite system since 210 ka: an investigation of factors controlling  
799 sedimentation. *EGU General Assembly*, 23-28 April 2017, Vienna, Austria, Vol. 19, 08963.

800 Lee, H., Beighley, R.E., Alsdorf, D., Jung, H.-C., Shum, C.K., Duan, J., Guo, J., Yamazaki, D., Andreadis, K.,  
801 2011. Characterization of terrestrial water dynamics in the Congo Basin using GRACE and satellite radar  
802 altimetry, *Remote Sens. Environ.* 115, 3530–3538, doi:10.1016/j.rse.2011.08.015.

803 Lee, H., Jung, H.C., Yuan, T., Beighley, R.E., Duan, J., 2014. Controls of terrestrial water storage changes over  
804 the central Congo Basin determined by integrating PALSAR ScanSAR, Envisat altimetry, and GRACE  
805 data, in *Remote Sensing of the Terrestrial Water Cycle*, AGU Geophys. Monogr. 206, edited by V.  
806 Lakshmi et al., pp. 117–129, John Wiley, Hoboken, N.J., doi:10.1002/9781118872086.

807 Lee, H., Yuan, T., Jung, H.C., Beighley, E., 2015. Mapping wetland water depths over the central Congo Basin  
808 using PALSAR ScanSAR, Envisat altimetry, and MODIS VCF data, *Remote Sens. Environ.* 159, 70–79.

809 Leturmy, P., Lucazeau, F., Brigaud, F., 2003. Dynamic interactions between the Gulf of Guinea passive margin  
810 and the Congo River drainage basin: 1. Morphology and mass balance. *J. Geophys. Res.* 108(B8), 2383,  
811 doi:10.1029/2002JB001927.

812 Leopold, L.B., Maddock, T., 1953. The Hydraulic Geometry of Stream Channels and Some Physiographic  
813 Implications. U.S. Geological Survey Professional Paper 252.

814 Lisiecki, L.E., Raymo, M.E., 2005. A Pliocene-Pleistocene stack of 57 globally distributed benthic  $\delta^{18}O$   
815 records. *Paleoceanography* 20, PA1003. doi:10.1029/2004PA001071

816 Maley, J., 1982. Dust, clouds, rain types and climatic variations in tropical North Africa. *Quat. Res.* 18, 1-16.

817 Maley, J., 1992. Mise en évidence d'une péjoration climatique entre ca. 2 500 et 2000 ans BP en Afrique  
818 tropicale humide. *Bull. Soc. Géol. France* 163, 363-365.

819 Maley, J., Brenac, P., Bigot, S., Moron, V., 2000. Le domaine forestier africain et ses marges : les transitions  
820 climatiques majeures à l'époque actuelle et au cours des derniers millénaires. In Servant, M., Servant-  
821 Vildary, S. (eds). *Dynamique à long terme des écosystèmes forestiers intertropicaux*, chapter 25,  
822 UNESCO.

823 Maley, J., Giresse, P., Doumenge, C., Favier, C., 2012. Comment on “Intensifying Weathering and Land Use in  
824 Iron Age Central Africa.” *Science* 337, 1040–1040. doi:10.1126/science.1221820

825 Marsset, T., Droz, L., 2010. REPRESAI\_LEG1 cruise, Pourquoi Pas? R/V. doi:10.17600/10030170

826 Marsset, T., Droz, L., Dennielou, B., Pichon, E., 2009. Cycles in the architecture of the Quaternary Zaïre  
827 turbidite system: a possible link with climate. *Extern. Controls Deep-Water Depositional Syst.* 89–106.

828 Martins, O., Probst, J.L., 1991. Biogeochemistry of major African rivers: Carbon and minerals transport, in  
829 Degens, E.T., Kempe, S., Richey J.E. (eds). *Biogeochemistry of Major World Rivers*. SCOPE 42, 127–  
830 156.

831 Métivier, F., Gaudemer, Y., 1999. Stability of output fluxes of large rivers in South and East Asia during the last  
832 2 million years: Implications on floodplain processes. *Basin Research* 11, 293–303, doi:10.1046/j.1365-  
833 2117.1999.00101.x

834 Matmon, A., Bierman, P.R., Larsen, M.C., Southworth, S., Pavich, M., Caffee, M., 2003. Temporally and  
835 spatially uniform rates of erosion in the southern Appalachian Great Smoky Mountains. *Geology* 31,  
836 155–158.

837 Meybeck, M., 2003. Global analysis of river systems: from Earth system controls to Anthropocene controls. *Phil.*  
838 *Trans. R. Soc. B* 358, 1935–1955.

839 Michalopoulos, P., Aller, R.C., 2004. Early diagenesis of biogenic silica in the Amazon delta : Alteration,  
840 authigenic clay formation, and storage. *Geochimica and Cosmochimica Acta* 68, 1061-1085.

841 Morehead, M.D., Syvitski, J., Hutton, E.W.H., Peckham, S.D., 2003. Modeling the temporal variability in the  
842 flux of sediment from ungauged river basins. *Global and Planetary Change* 39, 95-110.

843 Morin-Rivat, J., Fayolle, A., Gillet, J.-F., Bourland, N., Gourlet-Fleury, S., Oslisly, R., Bremond, L., Bentaleb,  
844 I., Beekman, H., Doucet, J.-L., 2014. New evidence of human activities during the Holocene in the  
845 lowland forests of the northern Congo basin. *Radiocarbon* 56(1), 209-220.

846 Neumann, J., 1955. Latitudinal variation of tropospheric temperature lapse rate. *Archiv für Meteorologie,*  
847 *Geophysik und Bioklimatologie, Serie A* 8(4), 351-353.

848 Neumann, K., Eggert, M.K.H., Oslisly, R., Clist, B., Denham, T., Maret, P. de, Ozainne, S., Hildebrand, E.,  
849 Bostoen, K., Salzmann, U., Schwartz, D., Eichhorn, B., Tchiengué, B., Höhn, A., 2012. Comment on  
850 “Intensifying Weathering and Land Use in Iron Age Central Africa.” *Science* 337, 1040–1040.  
851 doi:10.1126/science.1221747

852 Nkounkou, R.R., Probst, J.L., 1987. Hydrology and geochemistry of the Congo River system. In Degens E.T. et  
853 al. (eds). *Transport of Carbon and Minerals in Major World Rivers, Part 4*. Mitt. Geol-Paläont. Insti.  
854 Univ. Hambourg, SCOPE/UNEP Sond. 64, 483-508.

855 O’Loughlin, F., Trigg, M.A., Schumann, G.J.P., Bates, P.D., 2013. Hydraulic characterization of the middle  
856 reach of the Congo River, *Water Resource Research* 49, 5059–5070, doi:10.1002/wrcr.20398.

857 Osmaston, H.A., Harrison, S.P., 2005. Quaternary glaciations of Africa: A regional synthesis. *Quaternary*  
858 *International* 138-139, 32-54.

859 Peckham, S.D., 2009. Geomorphometry in RiverTools, In: Hengl, T., Reuter, H.I. (eds), *Geomorphometry:*  
860 *Concepts, Software and Applications*, Chapter 18, *Developments in Soil Science* 33, 411-430.

861 Pelletier, J.D., 2012. A spatially distributed model for the long-term suspended sediment discharge and delivery  
862 ratio of drainage basins. *Journal of Geophysical Research* 117, F02028, doi:10.1029/2011JF002129

863 Phillips, J.D., 2003. Alluvial storage and the long-term stability of sediment yields. *Basin Research* 15(2), 153–  
864 163, doi: 10.1046/j.1365-2117.2003.00204.x.

865 Picot, M., 2015. Cycles sédimentaires dans le système turbiditique ud Congo : nature et origine. PhD thesis,  
866 Université de Bretagne Occidentale, Brest. 368 pp.

867 Picot, M., Droz, L., Marsset, T., Dennielou, B., Bez, M., 2016. Controls on turbidite sedimentation: Insights  
868 from a quantitative approach of submarine channel and lobe architecture (Late Quaternary Congo Fan).  
869 *Marine and Petroleum Geology* 72, 423-446.

870 Picouet, C., Hingray, B., Olivry, J.C., 2001. Empirical and conceptual modelling of the suspended sediment  
871 dynamics in a large tropical African river: the Upper Niger River basin. *Journal of Hydrology* 250, 19-39.

872 Rabouille, C., Caprais, J.-C., Lansard, B., Crassous, P., Dedieu, K., Reyss, J.-L., Khripounoff, A., 2009. In situ  
873 measurements of sediment oxygen consumption and organic matter budget in the Southeast Atlantic  
874 continental margin close to the Congo Canyon. *Deep Sea Research Part II* 56, 2223–2238.

875 Regard, V., Carretier, S., Boeglin, J.-L., Ndam Ngoupayou, J.-R., Dzana, J.-G., Bedimo Bedimo, J.-P., Riotte, J.,  
876 Braun, J.-J., 2016. Denudation rates on cartonic landscapes: comparison between suspended and

877 dissolved fluxes, and  $^{10}\text{Be}$  analysis in the Nyong and Sanaga River basins, south Cameroon. *Earth*  
878 *Surface Processes and Landforms* 41, 1671-1683. doi: 10.1002/esp.3939

879 Reichenstein, M., Bahn, M., Ciais, P., Frank, D., Mahecha, M.D., Seneviratne, S.I., Zscheischler, J., Beer, C.,  
880 Buchmann, N., Frank, D.C., Papale, D., Rammig, A., Smith, P., Thonicke, K., van der Velde, M., Vicca,  
881 S., Walz, A., Wattenbach, M., 2013. Climate extremes and the carbon cycle. *Nature* 500, 287-295.

882 Rodier, J., 1964. Régimes hydrologiques de l'Afrique Noire à l'Ouest du Congo. *Mem. ORSTOM* 6, 137 pp.

883 Rogers, R.D., Schumm S.A., 1991. The effect of sparse vegetative cover on erosion and sediment yield, *J.*  
884 *Hydrol.* 123, 19 – 24. doi:10.1016/0022-1694(91)90065-P.

885 Roller, S., Wittmann, H., Kastowski, M., Hinderer, M., 2012. Erosion of the Rwenzori Mountains, East  
886 African Rift, from in situ-produced cosmogenic  $^{10}\text{Be}$ . *Journal of Geophysical Research* 117, F03003. DO  
887 I: 10.1029/2011JF002117

888 Rommerskirchen, F., Eglinton, G., Dupont, L., Rullkötter, J., 2006. Glacial/interglacial changes in southern  
889 Africa: Compound-specific  $\delta^{13}\text{C}$  land plant biomarker and pollen records from southeast Atlantic  
890 continental margin sediments. *Geochem. Geophys. Geosyst.* 7, Q08010. doi:10.1029/2005GC001223.

891 Savoye, B., 1998. ZAIANGO1 cruise, L'Atalante R/V. doi:10.17600/98010100

892 Savoye, B., Babonneau, N., Dennielou, B., Bez, M., 2009. Geological overview of the Angola–Congo margin,  
893 the Congo deep-sea fan and its submarine valleys. *Deep Sea Res. Part II Top. Stud. Oceanogr.* 56, 2169–  
894 2182. doi:10.1016/j.dsr2.2009.04.001

895 Schneider, R.R., Price, B., Müller, P.J., Kroon, D., Alexander, I., 1997. Monsoon related variations in Zaire  
896 (Congo) sediment load and influence of fluvial silicate supply on marine productivity in the east  
897 equatorial Atlantic during the last 200,000 years. *Paleoceanography* 12, 463–481.  
898 doi:10.1029/96PA03640

899 Sichingabula, H.M., (1999). Special study on sediment discharge and its consequence: analysis and results of  
900 discharge and sediment monitoring activities in the southern Lake Tanganyika basin, Zambia. Technical  
901 report number 4. UNDP/GEF. Dar es Salaam, Tanzania, 106 pp.

902 Simpson, G., Castellort, S., 2012. Model shows that rivers transmit high-frequency climate cycles to the  
903 sedimentary record. *Geology* 40(12), 1131-1134. doi:10.1130/G33451.1

904 Sionneau, T., Droz, L., Marsset, T., Dennielou, B., Bez, M., 2010. Congo-Zaire detrital supply variability during  
905 the last 200 ka: a possible explanation for the longitudinal migration of the Zaire fan depocenters. 18th  
906 International Sedimentological Congress, 26/09 to 01/10 2010, Mendoza (Argentina).

907 Spencer, R.G.M., Hernes, P.J., Dinga, B., Wabakanghanzi, J.N., Drake, T.W., Six, J., 2016. Origins, seasonality,  
908 and fluxes of organic matter in the Congo River, *Global Biogeochem. Cycles* 30,  
909 doi:10.1002/2016GB005427.

910 Summerfield, M.A., Hulton, N.J., 1994. Natural controls of fluvial denudation rates in major world drainage  
911 basins. *J. Geophys. Res. Solid Earth* 99, 13871–13883. doi:10.1029/94JB00715

912 Syvitski, J.P.M., Morehead, M.D., Nicholson, M., 1998. Hydrotrend: a climate-driven hydrologic-transport  
913 model for predicting discharge and sediment load to lakes or oceans. *Computers & Geosciences* 24, 51-  
914 68.

915 Syvitski, J.P.M., Morehead, M.D., 1999. Estimating river-sediment discharge to the ocean: application to the Eel  
916 margin, North California. *Marine Geology* 154,13–28.

917 Syvitski, J.P.M., Milliman, J., 2007. Geology, geography, and humans battle for dominance over the delivery of  
918 fluvial sediment to the coastal ocean. *The Journal of Geology* 115, 1–19.

919 Syvitski, J.P.M., Morehead, M.D., Bahr, D.B., Mulder, T., 2000. Estimating fluvial sediment transport: The  
920 rating parameters. *Water Resources Research* 36(9), 2747-2760.

921 Syvitski, J.P.M., Morehead, M.D., Nicholson, M., 1998. HydroTrend: a climate-driven hydrologic-transport  
922 model for predicting discharge and sediment load to lakes or the ocean. *Comput Geosci* 24(1), 51–68.

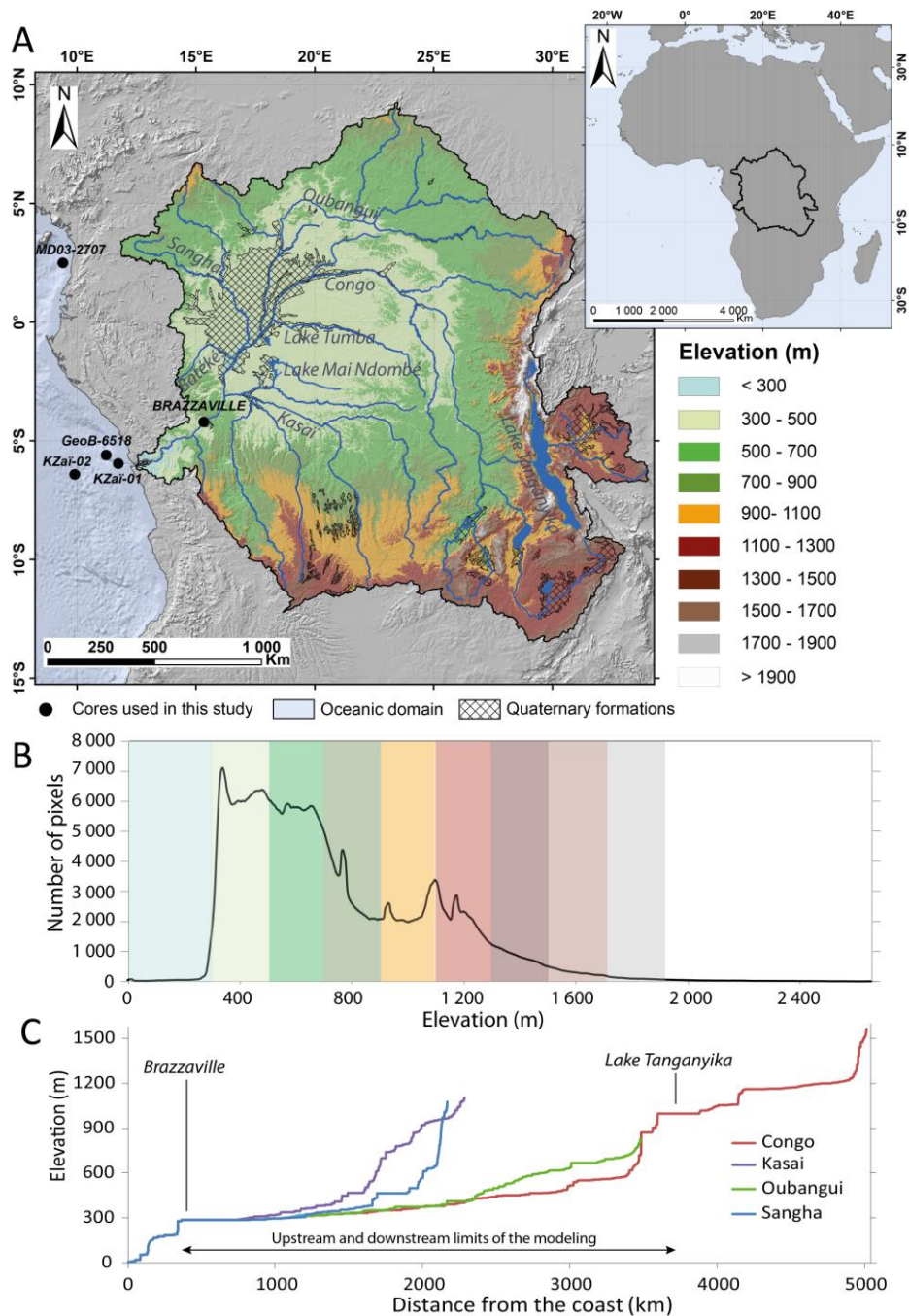
923 Syvitski, J.P.M., Vörösmarty, C.J., Kettner, A.J., Green, P., 2005. Impact of humans on the flux of terrestrial  
924 sediment to the global coastal ocean. *Science* 308, 376-380.

925 Syvitski, J.P.M., Kettner, A.J., Overeem, I., and Brakenridge, G.R., 2017. Latitudinal controls on siliciclastic  
926 sediment production and transport. *SEPM Special Publication No. 108*. Doi:  
927 <http://dx.doi.org/10.2110/sepm.sp.108.04>.

928 Thiry, M., 2000. Paleoclimatic interpretation of clay minerals in marine deposits: an outlook from the continental  
929 origin. *Earth Science Review* 49, 201–221.

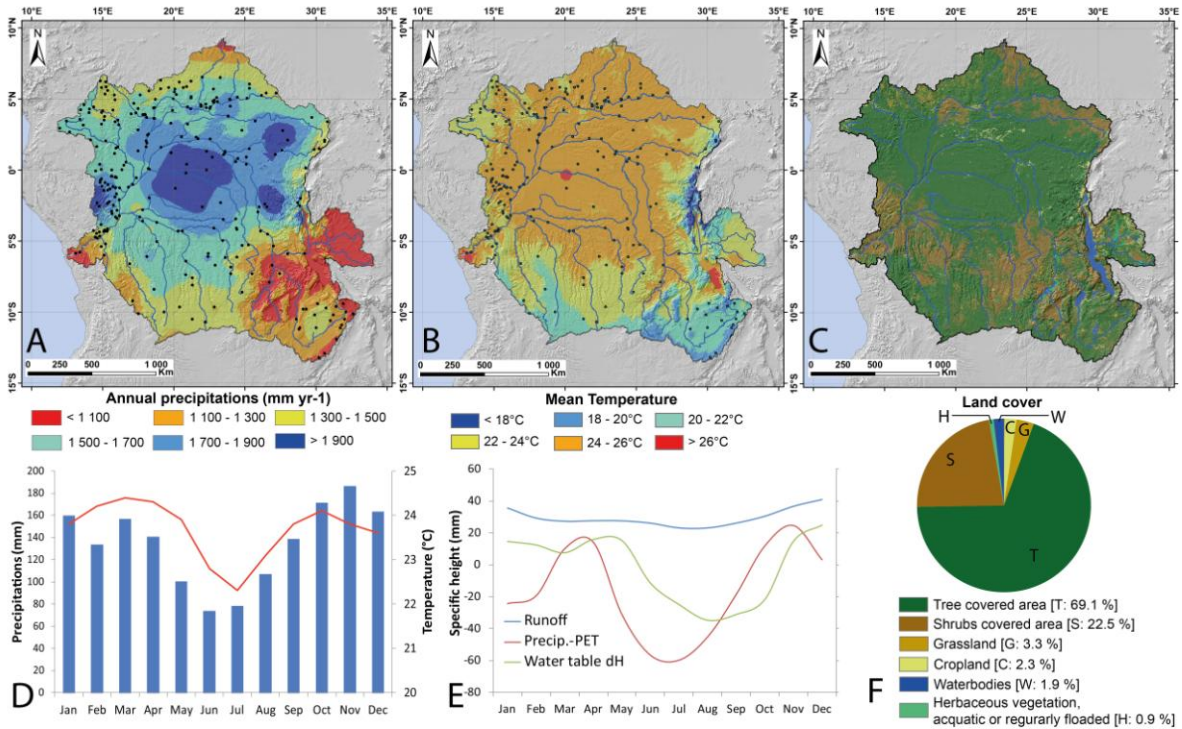


- 930 Tucker, C.J., 1979. Red and Photographic Infrared Linear Combinations for Monitoring Vegetation, Remote  
931 Sensing of Environment 8(2),127-150.
- 932 Vance, D., Bickle, M., Ivy-Ochs, S., Kubik, P.W., 2003. Erosion and exhumation in the Himalaya from  
933 cosmogenic isotope inventories of river sediments. Earth and Planetary Science Letters 206, 273–288.
- 934 Vangriesheim, A., Pierre, C., Aminot, A., Metzli, N., Baurand, F., Caprais, J.C., 2009. The influence of Congo  
935 River discharges in the surface and deep layers of the Gulf of Guinea, Deep Sea Research Part II 56,  
936 2183–2196.
- 937 Vanmaercke, M., Poesen, J., Broeckx, J., Nyssen, J., 2014. Sediment Yield in Africa. Earth-Science Reviews  
938 136, 350-368. doi: 10.1016/j.earscirev.2014.06.004
- 939 Vörösmarty C.J., Meybeck, M., Fekete, B., Sharma, K., 1997. The potential impact of neo-Castorization on  
940 sediment transport by the global network of rivers. In: Walling D., Probst, J.L. eds., Human Impact of  
941 erosion and sedimentation. IAHS Press, Wallingford, UK., 261–272.
- 942 Walling, D.E., 2006. Human impact on land–ocean sediment transfer by the world's rivers. Geomorphology 79,  
943 192–216.
- 944 Wang, J.-J., Adler, R.F., Huffman, G.J., Bolvin, D., 2014. An updated TRMM composite climatology of tropical  
945 rainfall and its validation. J. Climate 27, 273-284.
- 946 Weijers, J.W.H., Schefuss, E., Schouten, S., Sinninghe Damsté J.S., 2007. Coupled Thermal and Hydrological  
947 Evolution of Tropical Africa over the Last Deglaciation. Science 315, 1701-1704. doi:  
948 10.1126/science.1138131.
- 949 Weldeab, S., Lea, D.W., Schneider, R.R., Andersen. N., 2007. 155,000 Years of West African Monsoon and  
950 Ocean Thermal Evolution. Science 316, 1303-1307. doi: 10.1126/science.1140461
- 951 Wilby, R.L., Dalgleish, H.Y., Foster, I.D.L., 1997. The impact of weather patterns on historic and contemporary  
952 catchment sediment yields. Earth Surface Processes and Landforms 22, 353–63.
- 953 Winemiller, K.O. et al., 2016. Balancing hydropower and biodiversity in the Amazon, Congo and Mekong.  
954 Science 351, 128–129.
- 955 Wittmann, H., von Blanckenburg, F., Maurice, L., Guyot, J.-L., Filizola, N., Kubik, P.W., 2011. Sediment  
956 production and delivery in the Amazon River basin quantified by in situ-produced cosmogenic nuclides  
957 and recent river loads. GSA bulletin 123(5-6), 934-950. doi: 10.1130/B30317.1
- 958 Wotzka, H.P., 2006. Records of activity: radiocarbon and the structure of Iron Age settlement in Central Africa.  
959 In: Wotzka, H.P., ed. Grundlegungen. Beiträge zur europäischen und afrikanischen Archäologie für  
960 Manfred K.H. Eggert. Tübingen: Francke Attempto Verlag, 271–289.
- 961 Xie, Y., Sha, Z., Yu, M., 2008. Remote sensing imagery in vegetation mapping: a review. Journal of Plant  
962 Ecology 1(1), 9-23.
- 963 Xu, J.X., 2003. Sediment flux to the sea as influenced by changing human activities and precipitation: example  
964 of the Yellow River, China. Journal of Environmental Management 31(3), 328–41.
- 965 Zomer, R.J., Trabucco, A., Bossio, D.A., Verchot, L.V., 2008. Climate change mitigation: A spatial analysis of  
966 global land suitability for clean development mechanism afforestation and reforestation. Agriculture  
967 Ecosystems and Environment 126, 67-80.
- 968 Zhang, Q., Justice, C.O., Jiang, M., Brunner, J., Wilkie, D.S., 2006. A GIS-based assessment on the vulnerability  
969 and future extent of the tropical forests of the Congo basin. Environmental Monitoring and Assessment  
970 114, 107-121.
- 971 Zhu, Y.M., Lu, X.X., Zhou, Y., 2007. Suspended sediment flux modeling with artificial neural network: an  
972 example of the Longchuanjiang River in the upper Yangtze catchment, China. Geomorphology 84,111–  
973 125.
- 974



976

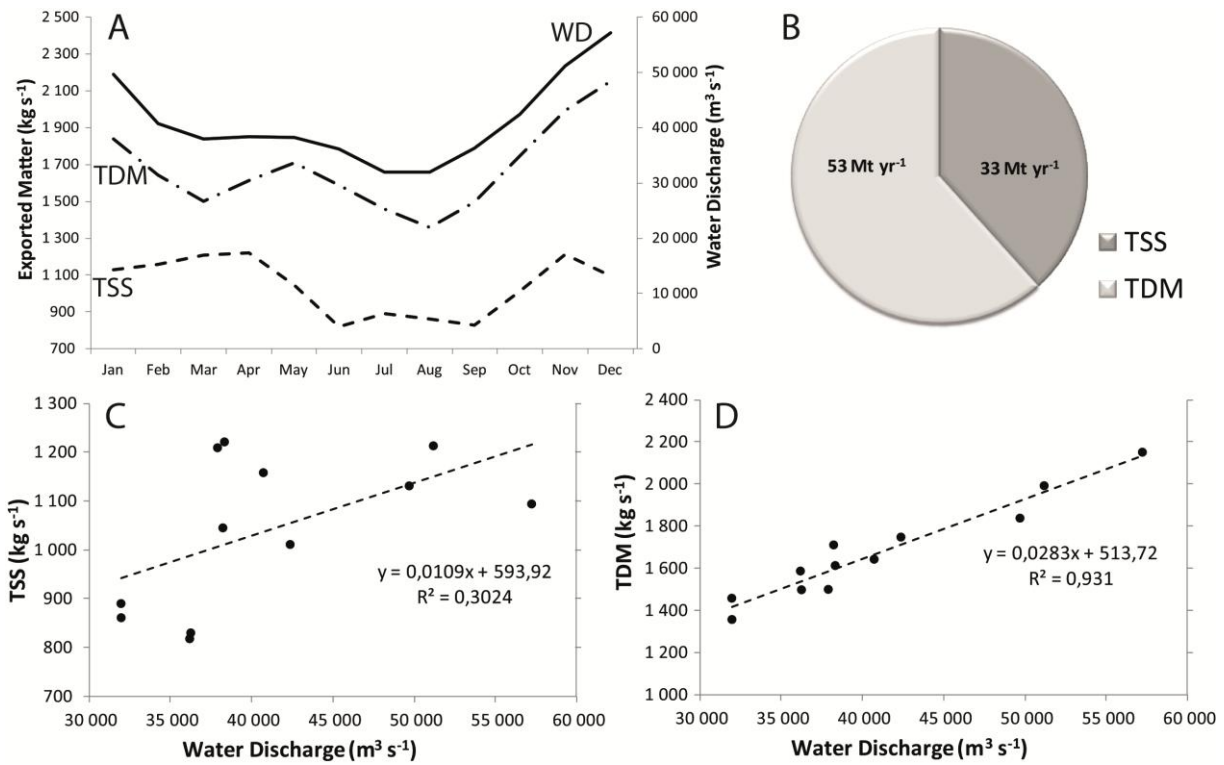
977 Figure 1: Geomorphological setting of the Congo catchment. A) Drainage basin represented by  
 978 elevation, where dark blue indicates the Congo River with its major tributaries and lakes, location of  
 979 datasets used and Quaternary deposits. B) Statistical distribution of elevation within the catchment. C)  
 980 Longitudinal profiles of the Congo River and its main tributaries, with upstream and downstream  
 981 boundaries of the modeling. Note that the knickpoint on the Congo River profile at Brazzaville  
 982 indicates that regressive erosion due to the successive marine oscillations in Quaternary does not affect  
 983 the morphology of the catchment above this point.



984

985 Figure 2: Environmental setting of the Congo catchment. A) Spatial distribution of annual  
 986 precipitations (data from Hijmans et al., 2005) and location of the SIEREM stations used for  
 987 calculation of temporal precipitation standard variation. B) Spatial distribution of mean annual  
 988 temperature (data from Hijmans et al., 2005). C) Spatial distribution of land cover (data from Latham  
 989 et al., 2014). D) Mean monthly precipitations (blue bars) and temperature (red line). E) Monthly water  
 990 balance, with runoff (blue) (data from Laraque et al., 2013), available water (precipitation minus  
 991 potential evapo-transpiration (PET; Zomer et al., 2008, in red) and variations in water table height  
 992 (from lakes-level satellite-monitoring; Crétaux et al., 2011; Becker et al., 2014, in green). F)  
 993 Quantitative repartition of land cover.

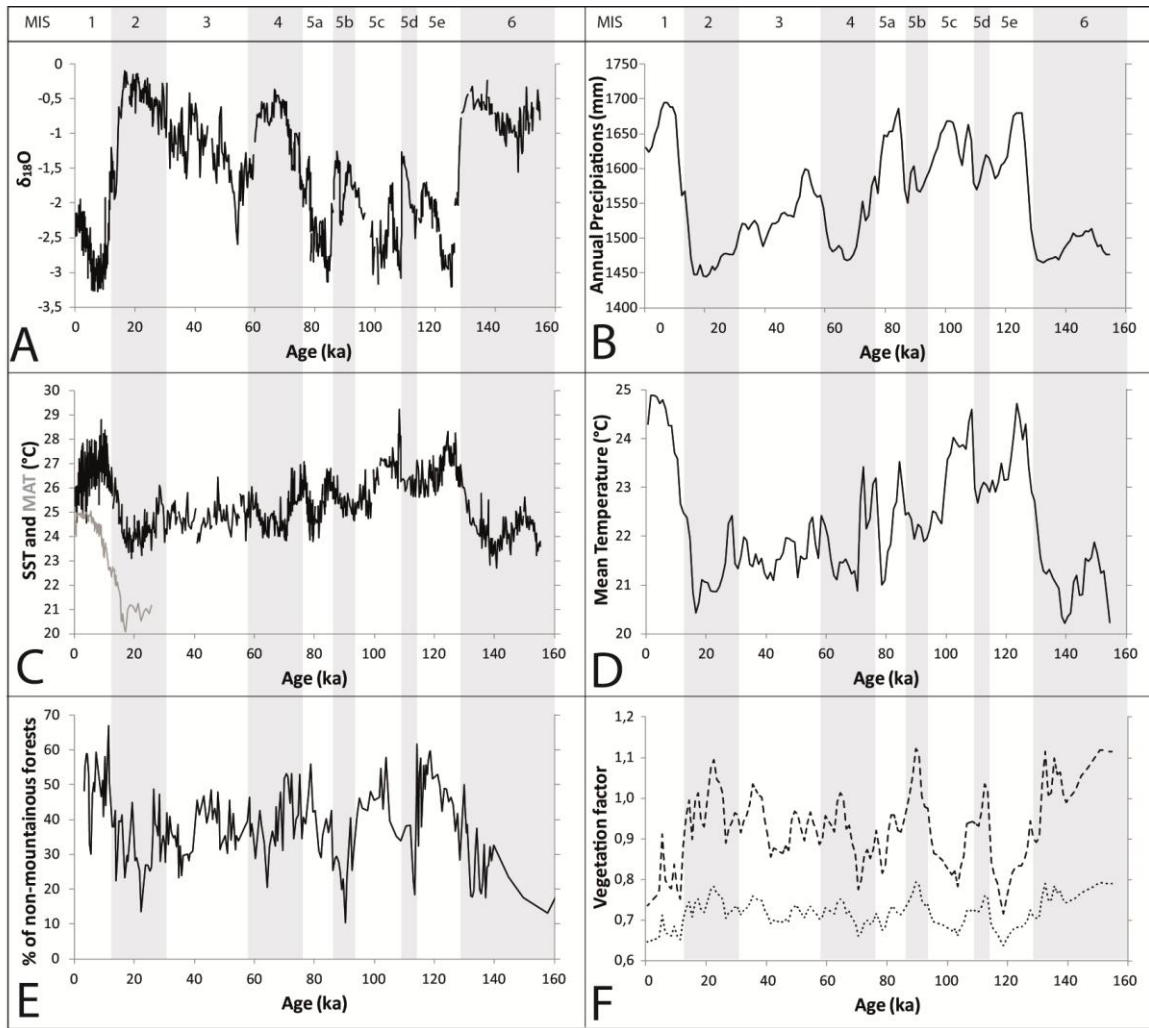
994



995

996 Figure 3: Mean monthly water and sediment discharge of the Congo watershed, in-situ monitored at  
 997 Brazzaville gauging station (from Laraque et al., 2013). A) Monthly water discharge (WD; solid line),  
 998 monthly Total Suspended Sediments (TSS; regular-dashed line), monthly Total Dissolved Matter  
 999 (TDM, dashed line with dots). B) Annual sediment yield (Total Suspended Sediments and Total  
 1000 Dissolved Matter, respectively) exported from the Congo catchment. C) Relation between mean  
 1001 monthly TSS and mean monthly water discharge. D) Relation between mean monthly TDM and mean  
 1002 monthly water discharge.

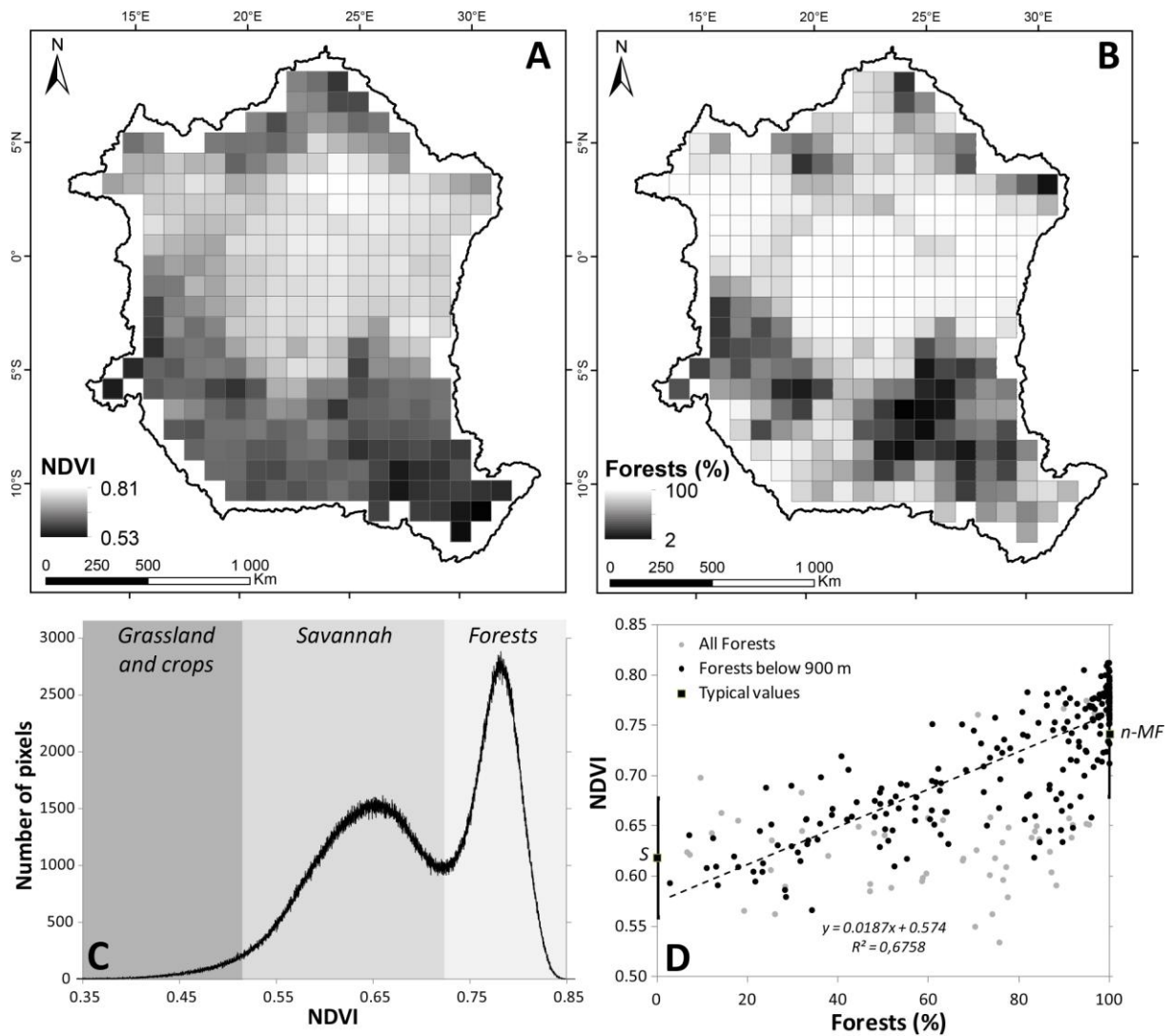
1003



1004

1005 Figure 4: Evolution of different marine proxies over the last 155 ka (A, C, E), used for the  
 1006 interpretation of environmental changes (B, D, F). A)  $\delta^{18}\text{O}$  curve of the MD03-2707 core which is  
 1007 located in the Guinea Gulf (Weldeab et al., 2007). B) Interpretation of  $\delta^{18}\text{O}$  data in terms of  
 1008 precipitation changes, since these data are interpreted as representative of the monsoon intensity  
 1009 (Weldeab et al., 2007; Caley et al., 2011). C) Sea Surface Temperature curve (SST, black line) of the  
 1010 MD03-2707 core (Weldeab et al., 2007) and Mean Atmospheric Temperature (MAT, grey line) of the  
 1011 GeoB6518-1 core (Weijers et al., 2007). D) Interpretation of SST and MAT in terms of mean  
 1012 catchment temperatures. For B and D, the calibration is performed to present-day (Hijmans et al.,  
 1013 2005) and the LGM (Gent et al., 2011) from global climatic model CCSM4 values and the data are  
 1014 smoothed by applying a mean value for: i) a 1 ka step for the 155 ka simulation, and ii) a 200 years  
 1015 step for the 23 ka simulation. E) Percentage of non-mountainous forests pollens for the KZai-02 core  
 1016 (Dalibard et al., 2014). F) Interpretation of non-mountainous forests pollens in terms of vegetation  
 1017 factor (method detailed in text). The dotted line represents the minimum value and the dashed line the  
 1018 maximum.

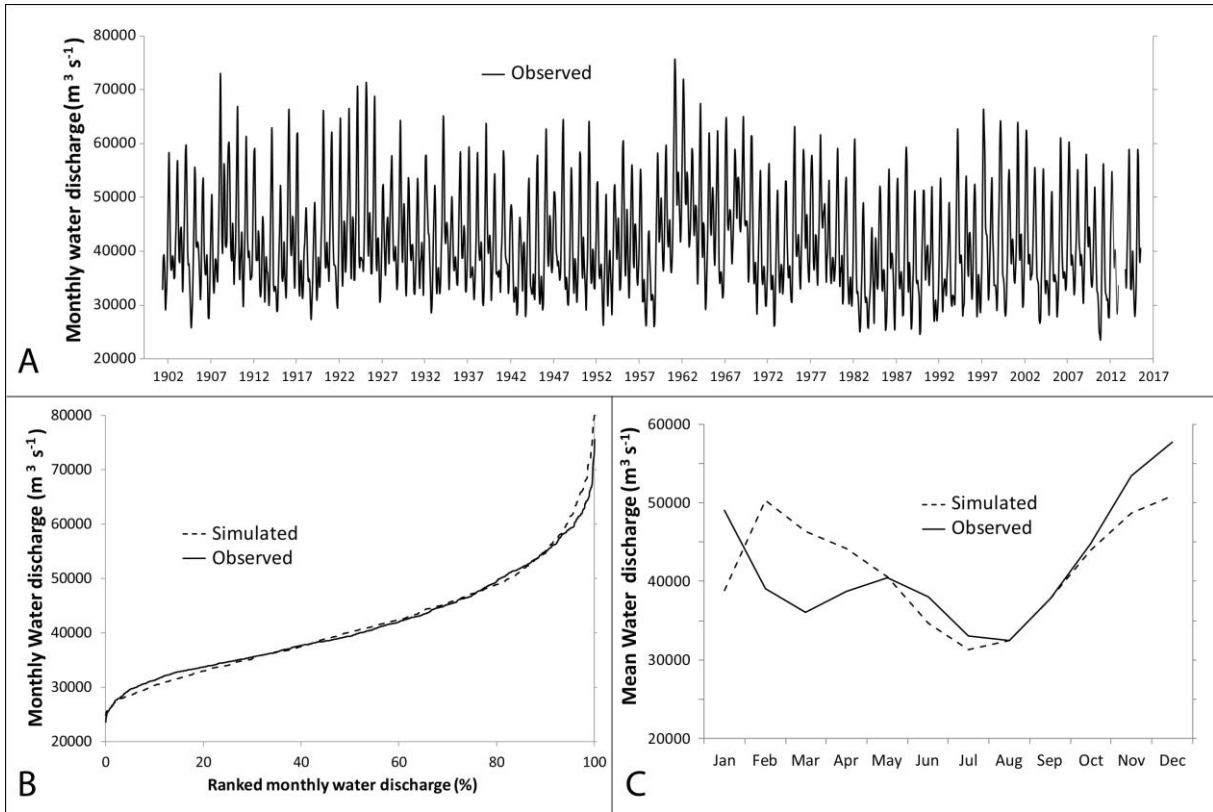
1019



1020

1021 Figure 5: The relation between NDVI (Normalized Difference Vegetation Index) and spatial Forest  
 1022 distribution. A) Mean annual NDVI averaged for 100 x 100 km tiles. B) Mean percentage of forests  
 1023 averaged for 100 x 100 km tiles. C) Statistical distribution of NDVI and type of land cover associated.  
 1024 D) Correlation between mean NDVI and mean percentage forest, averaged for 100 x 100 km tiles. The  
 1025 vertical black bars at 0 and 100 % correspond to the range of NDVI values for savannah (S) and non-  
 1026 mountainous forests (n-MF). Equation and  $R^2$  are given only for non-mountainous forests (black dots).

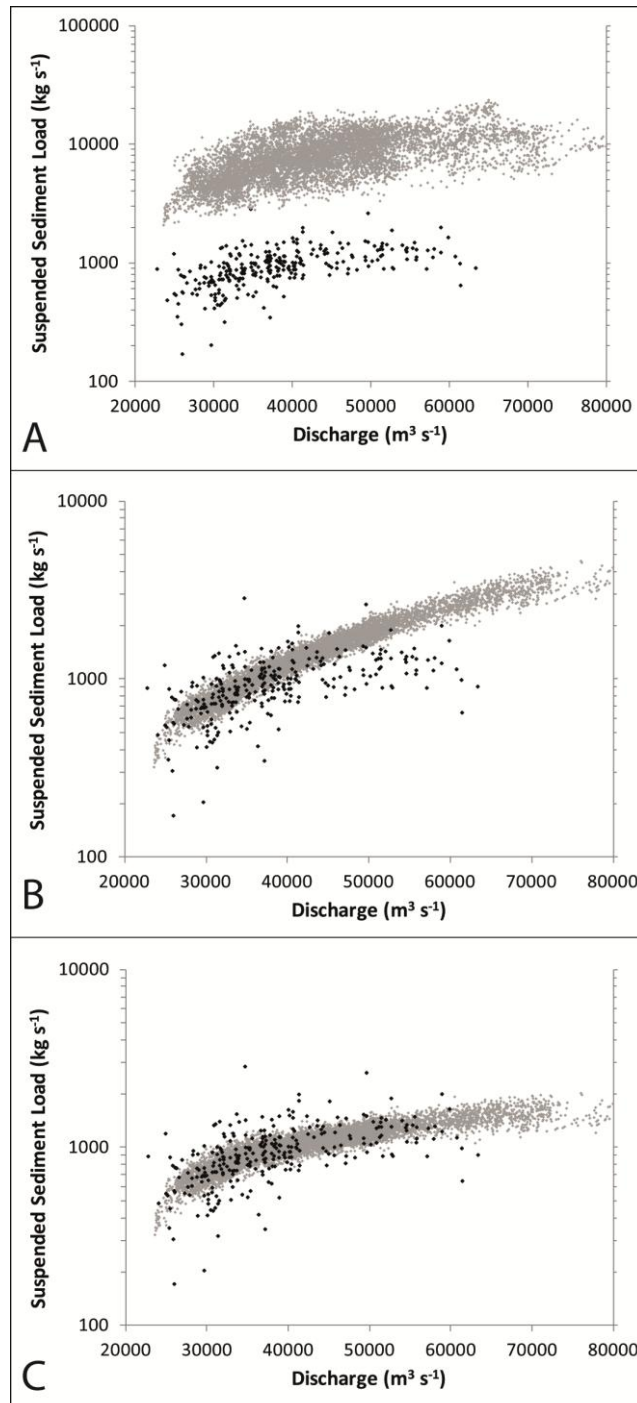
1027



1028

1029 Figure 6: Calibration of simulated water discharge with present-day data. A) Observed, 114 years of  
 1030 monthly discharge data at the Brazzaville gauging station (Laraque et al., 2013a; HYBAM, 2016). B)  
 1031 Ranked monthly observed (solid line) and simulated (dashed line) water discharge. C) Monthly  
 1032 observed and simulated mean water discharge. These data highlight the capability of the HydroTrend  
 1033 model to simulate realistic discharges for the Congo River at Brazzaville.

1034

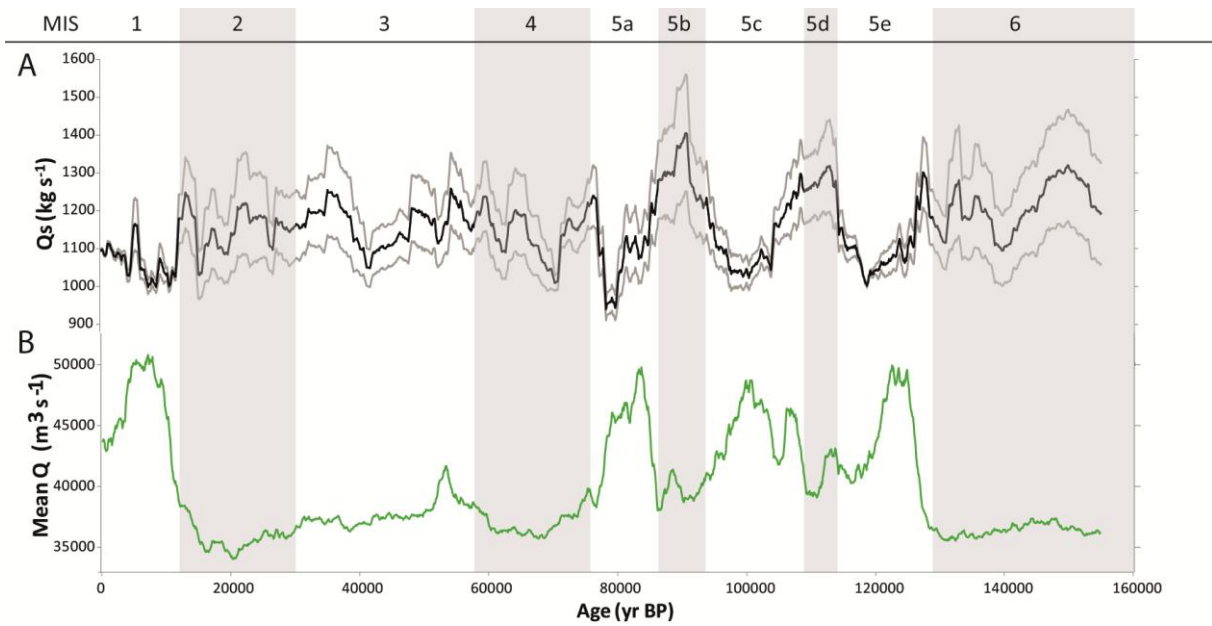


1035

1036 Figure 7: Calibration of simulated suspended sediment load with present-day observed data. The  
 1037 graphs A, B and C show the relation between suspended sediment load and water discharge. Observed  
 1038 data are represented as black dots; 20 years of daily simulated data are represented as grey dots. A)  
 1039 Simulations without trapping. B) Simulation including classic trapping (i.e. trapping by a lake) in the  
 1040 Cuvette Centrale. C) Simulation including classic and floodplain trapping when discharge exceed  
 1041 bankfull discharge ( $>33,000 \text{ m}^3 \text{ s}^{-1}$  for the best fit). To match simulated to observed data, sediment  
 1042 trapping by involving at least two distinct processes is needed.

1043

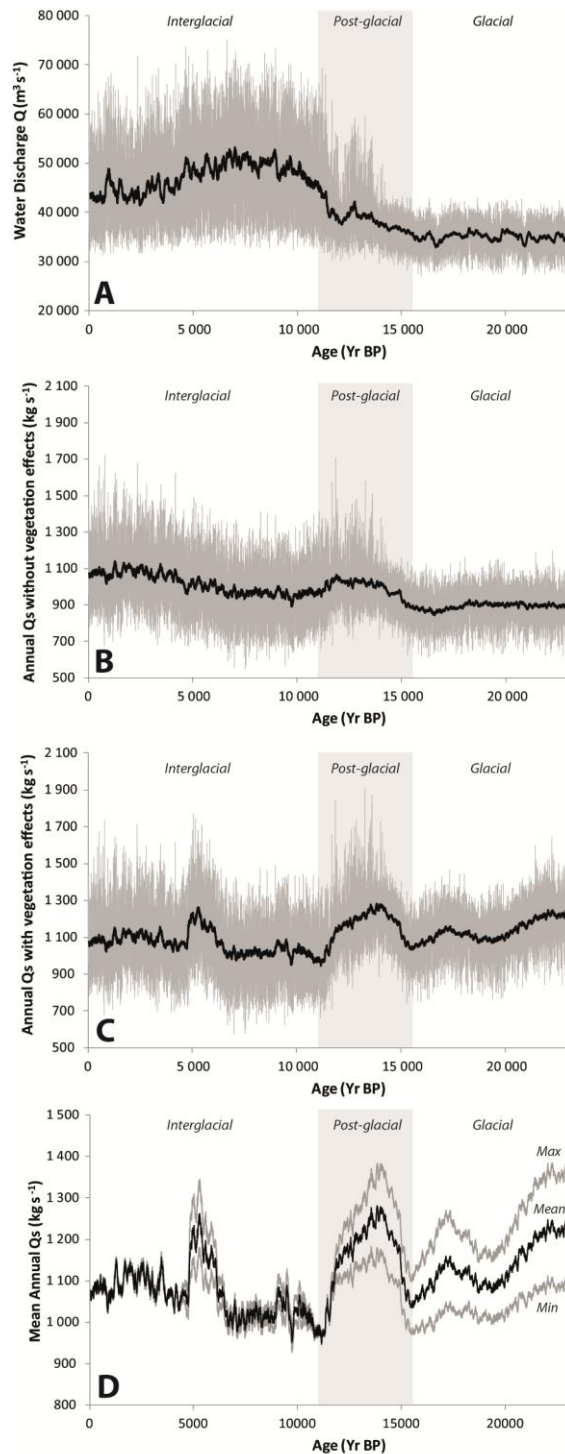




1044

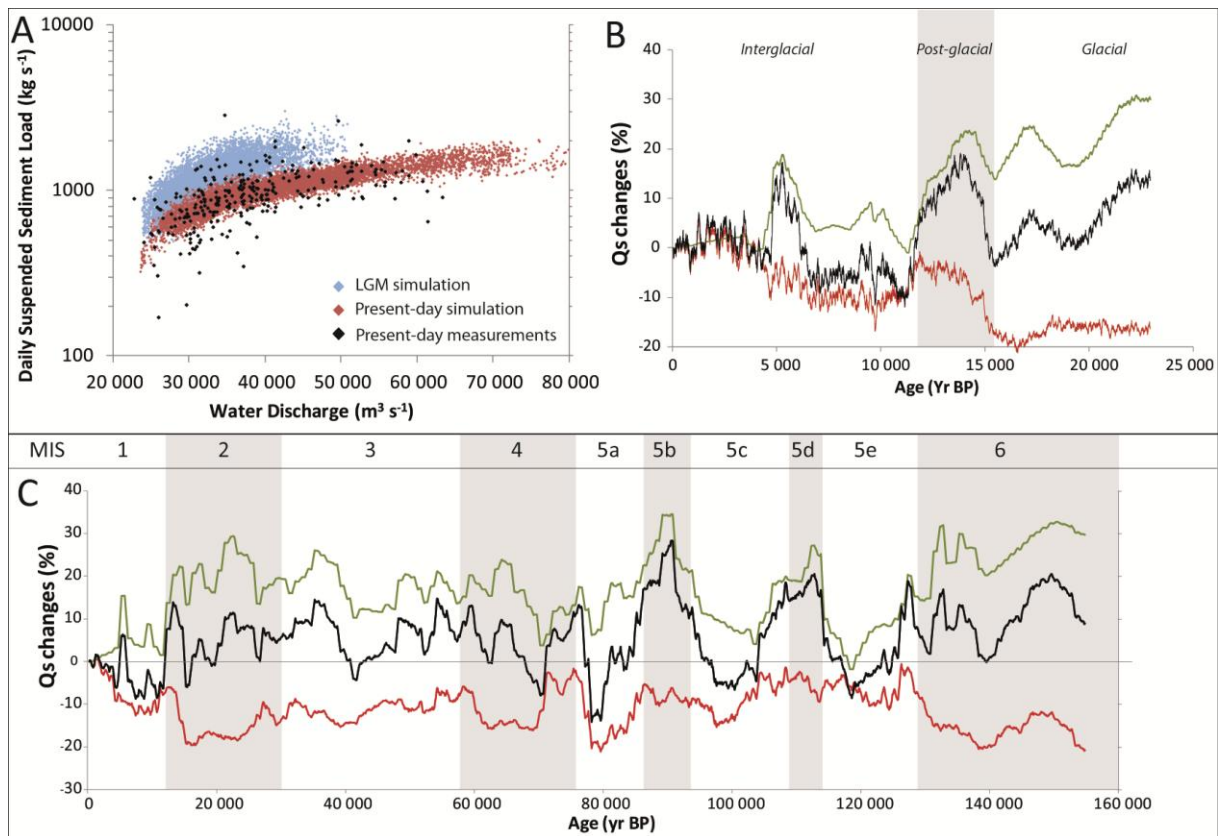
1045 Figure 8: HydroTrend simulations of sediment load and water discharge over the last 155 ka. A)  
 1046 Simulated suspended sediment load evolution (Qs). The black curve corresponds to the mean sediment  
 1047 load, grey curves are the minimum and maximum with respect to vegetation index. B) Simulated  
 1048 water discharge. Curves A and B are running averages over 500 years of mean annual data simulated.

1049



1050

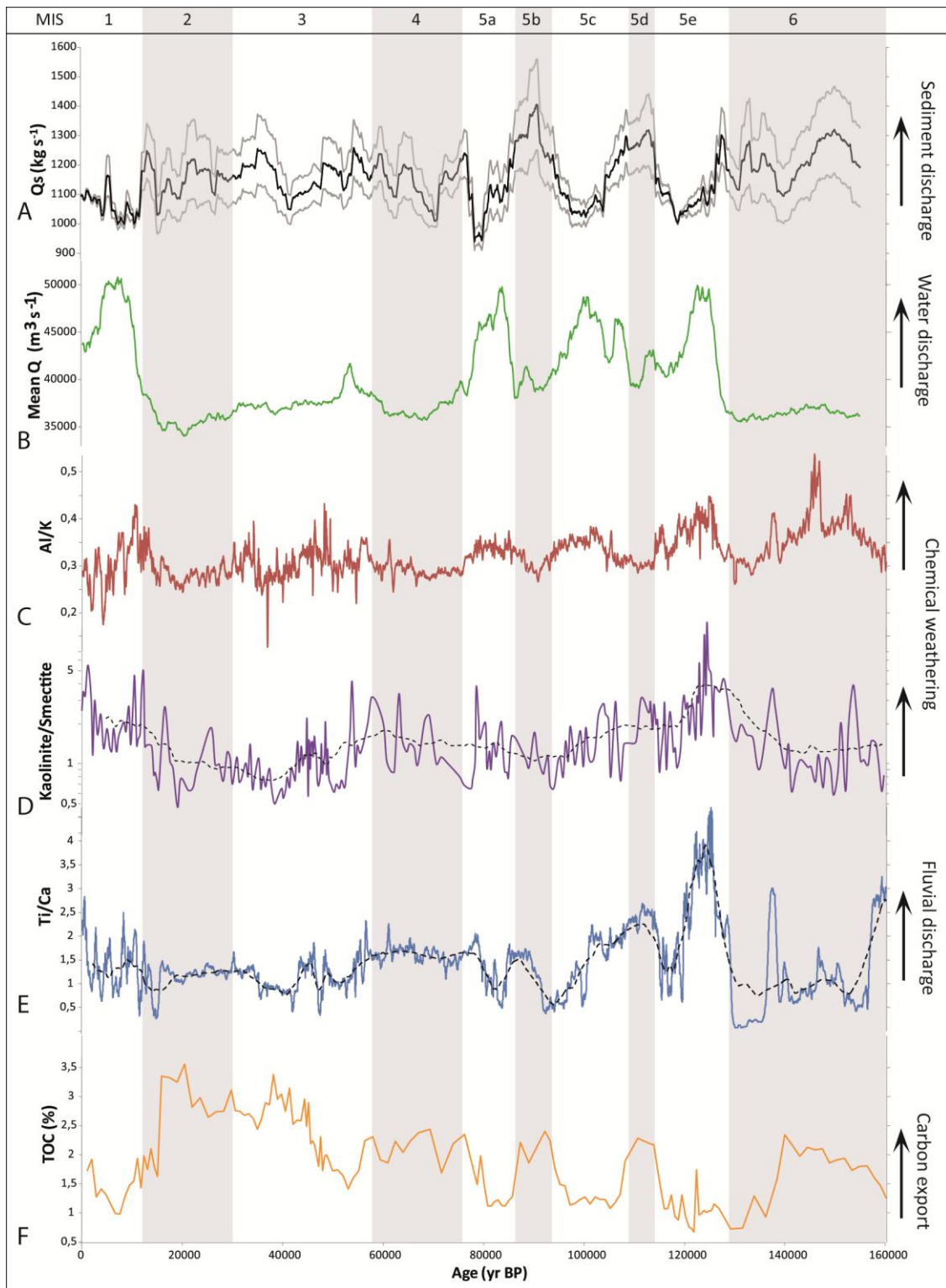
1051 Figure 9: Water and suspended sediment simulation results focused over the last 23 ka. Gray curves  
 1052 represent annual data, while black curves are running means over 100 years. Three climatic periods  
 1053 (interglacial, post-glacial and glacial) are individualized by the light gray/white bands in background.  
 1054 A) Water discharge. B) Suspended sediment load without taking into account vegetation changes. C)  
 1055 Mean suspended sediment load taking into account vegetation changes. D) Running mean over 100  
 1056 years of minimum (lower grey line), maximum (upper grey line) and mean (black line) suspended  
 1057 sediment load.



1058

1059 Figure 10: A) Relation between suspended sediment load and water discharge during present-day  
 1060 (observed data are represented with black triangles; 20 years of daily simulated data are represented  
 1061 with red triangles) and LGM conditions (20 years of daily simulation data are represented in blue). B)  
 1062 Deciphering the effect of only climate (without vegetation changes over time) (red curve) and only  
 1063 vegetation (green curve), and combined on mean suspended sediment load (black curve) for the last 23  
 1064 ka. On the background, the light gray period correspond to post-glacial stage. C) Deciphering the  
 1065 effect of climate and vegetation over the last 155 ka. The caption is the same as B except that light  
 1066 gray periods correspond to cold climatic stages.

1067



1068

1069 Figure 11: Comparisons of HydroTrend simulations with available offshore proxies related to  
 1070 sediment supply. A) and B) see caption in Fig. 8. C) Al/K semi-quantitative ratio measured with a  
 1071 XRF (Hatin et al., 2017). D) Log of Kaolinite/Smectite ratio (Sionneau et al., 2010). E) Ti/Ca semi-  
 1072 quantitative ratio measured with a XRF. F) Total Organic Carbon (TOC). Curves C to F were drawn  
 1073 from XRF measurements from core KZai-02 (location in Figure 1). The dashed lines in D and E are  
 1074 running averages. In the background, the light gray periods correspond to cold climatic stages.

1075 **Table captions**

1076 Table 1: Values of parameters used in simulations.

Parameters	Value	Unit	Référence
Present-day yearly temperature	24.6	°C	Alsdorf et al., 2016
Standard deviation of yearly temperature	1.44	°C	Alsdorf et al., 2016
Present-day yearly precipitation	1630.1	mm	Alsdorf et al., 2016
Standard deviation of yearly precipitation	563	mm	Alsdorf et al., 2016
Precipitation mass balance coefficient	1		Syvitski et al., 1998
Distribution exponential	1.7		Syvitski et al., 1998
Distribution range	9		Syvitski et al., 1998
Constant annual baseflow	22000	m <sup>3</sup> .s <sup>-1</sup>	Alsdorf et al., 2016
Monthly Temperature	see Fig. 2D	°C	Hijmans et al., 2005
Monthly Precipitation	see Fig. 2D	mm	Hijmans et al., 2005
Lapse rate	6.4	°C.km <sup>-1</sup>	Neumann, 1955
ELA start	4500	m	Osmaston and Harrison, 2005
Dry precipitation evaporation fraction	0		Syvitski et al., 1998
Average slope of the river bed delta	0.000183625		DEM
River lenght	4700	km	DEM
Volume of reservoirs	1000	km <sup>3</sup>	DEM and our calibration
Altitude of reservoirs	290	m	DEM
Velocity coefficient (k)	0.56		Leopold and Maddock, 1953
Velocity exponent (m)	0.1		Leopold and Maddock, 1953
Width coefficient (a)	6.62		Leopold and Maddock, 1953
Width exponent (b)	0.61		Leopold and Maddock, 1953
Average velocity	1.23	m <sup>3</sup> .s <sup>-1</sup>	Laraque et al., 1995
Maximum groundwater storage	6.10 <sup>11</sup>	m <sup>3</sup>	Cretaux et al., 2011; Becker et al., 2014
Minimum groundwater storage	10 <sup>11</sup>	m <sup>3</sup>	Cretaux et al., 2011; Becker et al., 2014
Initial groundwater storage	3.5.10 <sup>11</sup>	m <sup>3</sup>	Cretaux et al., 2011; Becker et al., 2014
Groundwater coefficient	15000	m <sup>3</sup> .s <sup>-1</sup>	Cretaux et al., 2011; Becker et al., 2014
Groundwater exponent	1.4		Cretaux et al., 2011; Becker et al., 2014
Saturated hydraulic conductivity	315	mm.day <sup>-1</sup>	Bear, 1972 and our calibration
Latitude of the outlet	15.3 N		DEM
Longitude of the outlet	4.283 W		DEM
Lithology factor (L)	1		Syvitski and Milliman, 2007
Anthropogenic factor	1		Syvitski and Milliman, 2007
Landcover factor	0.6444-0.7325		our calibration (min-max)
Bankfull discharge	33000	m <sup>3</sup> .s <sup>-1</sup>	our calibration
Altitude of bankfull discharge	350	m	DEM

1077

1078

1079

1080